Western Michigan University
ScholarWorks at WMU

Dissertations | Graduate College

12-2019

Simultaneous X-Ray Emission Accompanying Two Electron Capture for Fluorine on Gas Targets

David S. La Mantia
Western Michigan University, lamantiads@gmail.com

Follow this and additional works at: https://scholarworks.wmich.edu/dissertations

 Part of the Physics Commons

Recommended Citation

La Mantia, David S., "Simultaneous X-Ray Emission Accompanying Two Electron Capture for Fluorine on Gas Targets" (2019). *Dissertations*. 3543.
https://scholarworks.wmich.edu/dissertations/3543

This Dissertation-Open Access is brought to you for free and open access by the Graduate College at ScholarWorks at WMU. It has been accepted for inclusion in Dissertations by an authorized administrator of ScholarWorks at WMU. For more information, please contact wmu-scholarworks@wmich.edu.

SIMULTANEOUS X-RAY EMISSION ACCOMPANYING TWO ELECTRON CAPTURE FOR FLUORINE ON GAS TARGETS

by

David S. La Mantia

A dissertation submitted to the Graduate College
in partial fulfillment of the requirements
for the degree of Doctor of Philosophy
Physics
Western Michigan University
December 2019

Doctoral Committee:

John A. Tanis, Ph.D., Chair
Thomas Gorczyca, Ph.D.
Asghar Kayani, Ph.D.
Anna Simon, Ph.D.
Andrzej Warczak, Ph.D.

© 2019 David S. La Mantia

Acknowledgements

I would first and foremost like to thank my principal advisor Dr. John Tanis for his encouragement, patience, and assistance throughout the Ph.D. process. I owe my proficiencies in the laboratory, data analysis, and research presentation to his guidance. The experiences I have gained professionally and personally over the last five years are due to his support.

I would also like to express my sincere gratitude to Dr. Andrzej Warczak for sponsoring my stay in Poland at the Jagiellonian University and for serving on my Ph.D. committee. I have gained a deep appreciation of Polish culture and feel the year spent in his lab has advanced my prowess in the field of atomic physics as much as any experience I have had.

The operation of the accelerator and execution of the project would not have been possible without the training and guidance of two people: Dr. Asghar Kayani and Mr. Allan Kern. Both men are a pleasure to work with and were invaluable to my dissertation research. I would also like to thank Drs. Tom Gorczyca and Anna Simon for their time and effort in serving on my Ph.D. committee and their valuable comments throughout this process.

The work produced at WMU certainly would not have been possible without the significant efforts of Dr. Nuwan Kumara. I thank him especially for his willingness to take shifts when running the accelerator. I thank also the contributions of the graduate and undergraduate students who contributed to the project over its long life.

I would like to thank the Department of Physics faculty, staff, and administration for their patience and support. The circumstances of my studies became quite demanding for them at times and they were always there for me.

There are too many friends and family to name who have supported me on this journey. I would thank a few by name. First are those who are no longer here to share in this triumph: my mother Nancy La Mantia and her father James La Mantia. I miss you both. Lastly, I thank most my grandparents Susan and Edward Harrison, Gram and Ha. I would have been nothing without you in my life.

David S. La Mantia

SIMULTANEOUS X-RAY EMISSION ACCOMPANYING TWO ELECTRON CAPTURE FOR FLUORINE ON GAS TARGETS

David S. La Mantia, Ph.D.

Western Michigan University, 2019

The collision between a charged ion and an atom resulting in the capture of two electrons, simultaneous with the emission of a single photon is referred to as radiative double electron capture (RDEC). For ion-atom collisions, this process can be considered the inverse of double photoionization. The study of either process, where just two electrons are involved without influence from neighboring electrons, promises new insight into electron correlation and the role it plays in quantum mechanics. Such a study for photoionization has not yet been done experimentally for two-electron ions because the only target system for which two electrons are available is atomic helium. The ability to gain information on pure correlation will thus be important to fundamental studies of RDEC and double photoionization and to applications in astrophysics and in plasma physics. RDEC is related to the well-known process of radiative electron capture (REC), in which a single electron is captured to a bound state with the simultaneous emission of a photon, considered the ion-atom analog of radiative recombination.

Several attempts have been made to observe RDEC experimentally but without definitive results using mid- to high-Z, high-energy projectiles on thin-foil and gaseous targets. Several theoretical studies have been performed over the last 25 years, with recent results suggesting that mid-Z, lower-energy projectiles would yield better results by giving larger cross sections. The first successful observation of RDEC was performed at Western Michigan University using 2.38 MeV/u O^{8+} projectiles incident on thin-foil carbon targets. This result was followed by measurements for 2.21 MeV/u F^{9+} also on carbon foils, which however suffered

from contaminants in the target. Multiple-collision effects were present as expected for thin-foil targets, causing the RDEC events to be distributed over the double and single capture channels. These previous measurements provide the motivation for the present RDEC work with gaseous targets.

Presented in this study are the results for RDEC by 2.11 MeV/u fully-stripped, and also one-electron fluorine ions colliding with N_2 and Ne. Cross sections for both projectiles are determined and compared with theoretical calculations to the extent possible, as well as with each other. The measurements were done under single-collision conditions to prevent complication from multiple collision events. High purity target gases were used to minimize the effects of contaminants.

Contents

List of Tables

List of Figures

1 Introduction

Ion-atom collisions provide a tool for the investigation of fundamental processes in atomic physics. This is especially true for the analysis of specific processes in which electrons are involved. The use of highly-stripped, swift ion projectiles and pure gaseous targets makes it possible to isolate and enhance the results in many instances. Specifically, charge-changing cross sections are of particular importance in testing the validity of physical theories.

The most fundamental collision process pertaining to atomic physics occurs when a photon strikes an atom. The atom may then absorb the photon energy, and can subsequently eject one or more electrons. This process is termed photoionization. Observing photoionization in the laboratory can be quite challenging to realize, depending on the energy of the photon and the target species or ionization state. Practical challenges can include manipulating the target, the intensity of the photon beam, or creating collinear photon and atom beams.

In practice, it is often far easier to apply the principle of detailed balance [1, 2] to consider the time-inverse of these processes. For photoionization, the time-inversed process would be radiative recombination [3], where an electron is captured from the continuum to a vacancy in an ion with the simultaneous emission of a photon. Taking the ion-atom analog of this process one arrives at radiative electron capture [4, 5], where one electron is captured from a bound state in the target atom to a bound state in the projectile ion with the simultaneous emission of a photon.

While the processes mentioned concern the liberation or capture of a single electron, two (or more) electrons may be involved. Double photoionization has been of interest to theorists and experimentalists alike for decades. For a single photon to strike a target and liberate two electrons, the electrons must necessarily interact in some way. This interaction is termed electron correlation. Double photonionization has yet to be studied for two-electron systems other than atomic He. This is due to the technical challenges involved in creating collinear beams of photons and ions of sufficient intensity. More readily realizable experimentally

is the time-inversed, ion-atom analog of this process, known as radiative double electron capture (RDEC) [6]. Precisely, RDEC is the capture of two electrons from bound states in the target to bound states in the projectile ion with the simultaneous emission of a single photon.

Several attempts have been made to observe RDEC [7, 8, 9] without definitive results using mid- to high-Z, high-energy projectiles on thin-foil and gaseous targets. Theoretical studies [10, 11] and recent results [12, 13] suggest that mid-Z, lower-energy projectiles would yield better results by giving larger cross sections. The first successful experimental observation of RDEC was performed for 2.38 MeV/u O^{8+} projectiles [14] incident on thin-foil carbon, followed by measurements for 2.11 MeV/u F^{9+} also on carbon [15], which however suffered from contaminants in the target. Multiple-collision effects were present as expected for thin-foil targets, causing the RDEC events to be distributed over the double and, more dominantly, single capture outgoing channels, raising uncertainty in the interpretation of these O^{8+} and F^{9+} results.

The work contained herein begins in Chapter 2 with descriptions of the most fundamental atomic collision processes. Attention is given also to relevant background processes and resonant capture that may occur. A description of radiative electron capture then follows. Finally, radiative double electron capture is defined and a detailed description of previous experimental searches for the process and theoretical considerations is given. Chapter 3 describes the experimental apparatus, including the tandem Van de Graaff accelerator facility at Western Michigan University, target configuration, and data acquisition system. Chapter 4 describes the data analysis and results. The dissertation concludes with a discussion of the results in Chapter 5.

2 Atomic Collision Processes

2.1 Fundamental Atomic Processes

While there is a large number of atomic collisional processes that exist, the following are the most pertinent to the research performed for this dissertation. The first atomic collision process to be studied in depth historically was that of photoionization (PI) as it relates to the photoelectric effect. This effect was first observed by Hertz in 1887 [16] when it was found that electrodes created a spark more readily when bombarded with an ultraviolet light source. Einstein theorized in 1905 [17] that light consists of discrete packets of energy explaining the photoelectric effect, for which he was awarded the Nobel Prize in 1921. Photoionization is a collision process where an atom or molecule absorbs a photon and one or more of its bound electrons are ejected into the continuum, as shown in Fig. 1, leaving the atom or molecule in an ionized state (non-zero net charge).

The PI process can, of course, take place multiple times within an atom. An interesting process occurs when one photon transfers its energy to an atom with the emission of two electrons, termed double photoionization (DPI), also shown in Fig. 1. Quantum mechanics states that in the low-field regime a single light quantum can interact with a single photon only. For two electrons to be ejected into the continuum from an atom absorbing a single photon, the electrons must interact in some way. This interaction is termed electron correlation and is of fundamental interest for testing the basic tenets of quantum mechanics. These ionization processes may be reversed in time, where an electron is captured to an ion and a photon is emitted.

2.2 Background Processes

An important factor in ion-atom collisions is the electron-nucleus interaction via the Coulomb force. A charged particle traveling through an electric field will necessarily feel a force and its trajectory will change. Whenever a charged particle travels in a path that is not a

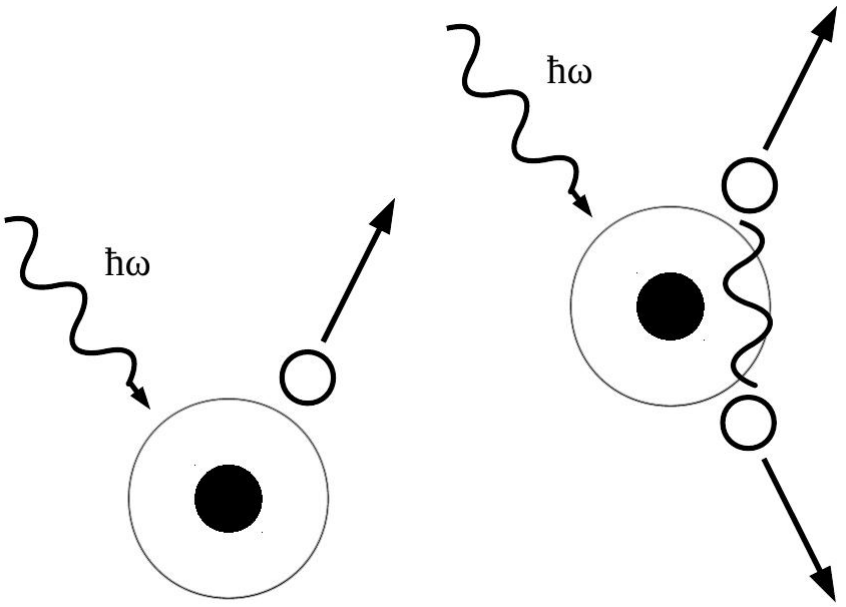

Figure 1: Single and Double Photoionization

straight line it is accelerated by definition and will emit radiation. This effect is known as bremsstrahlung ("braking radiation" in German) [18] and can be a significant background effect, especially in dense targets.

Bremsstrahlung can be present from both the projectile ions and the ejected target electrons. The total power radiated from classical bremsstrahlung is proportional to γ^4 when $\frac{d\vec{v}}{dt}$ is perpendicular to $\vec{v}$ or γ^6 when $\frac{d\vec{v}}{dt}$ is parallel to $\vec{v}$ [19], where $\gamma = \frac{1}{\sqrt{1-\frac{v^2}{c^2}}}$ is the Lorentz factor. The energy-momentum relation states $E^2 = (pc)^2 + (m_0c^2)^2 = (\gamma mc^2)^2$, so $\gamma \propto m^{-1}$. This leads to the total radiated power being $\propto m^{-4}$ or m^{-6}. The nucleus is much heavier than any ejected electron, so for any orientation of acceleration and velocity the so-called quasifree or secondary electron bremsstrahlung (SEB) processes will dominate over the nucleus-nucleus or atomic bremsstrahlung processes.

The emitted radiation has an energy maximum with T_{SEB} equal to maximum energy transfer from the projectile to the free electron [20]:

$$T_{SEB} = 4 * T_r = 4 * \frac{1}{2} m_e v_p^2 = 4 * (\frac{m_e}{M_p}) E_p$$

where T_r is the maximum kinetic energy of the involved electron, m_e is the electron mass, v_p is the projectile velocity, M_p is the projectile mass, and E_p is the projectile energy. For projectiles in the MeV energy range this radiation can be significant in the x-ray spectrum. In the context of this study, however, the target densities are quite low and the timing techniques employed eliminate this effect in the coincidence spectra.

2.3 Resonant Electron Capture

The observation of emitted photons is central to the work presented herein. It should be noted that the projectile may capture an electron without the emission of a photon. The energy of the captured electron(s) must go somewhere and either results in the promotion of one or more bound-state projectile electrons (termed resonant transfer excitation [21, 22, 23]) or is transferred to the kinetic energy of the collision constituents (termed nonradiative electron capture). In the former case a photon attributed to the projectile can be emitted making the process similar to the electron-ion collision process called dielectronic recombination [24, 25]. In the latter case no photon is emitted directly, but the subsequent relaxation of an electron captured to an excited state will radiate a photon or eject another electron. Nonradiative electron capture (NREC) occurs primarily for low velocities and when the velocity of the projectile matches the velocity of the captured electron ($v_p \approx v_e$). When $v_p \gg v_e$, the NREC cross section scales as [26]

$$\sigma_{\mathrm{NREC}} \propto \frac{Z_t^5 Z_p}{v_p^{12}} \tag{1}$$

where Z_t is the atomic number of the target and Z_p is the atomic number of the projectile. Regardless, these processes will not contribute or distract from the processes of interest described below.

2.4 Radiative Electron Capture

Radiative electron capture (REC) is a well-understood process in heavy ion-atom collisions. This process has been studied extensively over the last half century, both experimentally [4, 5, 27, 28, 29, 30, 31, 32] and theoretically [33, 34, 35, 36, 37]. REC is a one-step process in which a bound electron from the target atom is captured to a bound state of the projectile ion with the simultaneous emission of a photon, as seen in the energy schematic in Fig. 2. The emitted energy is therefore given as:

$$E_{REC} = K_t + B_p - B_t + \vec{v} \cdot \vec{p} \tag{2}$$

where K_t is the kinetic energy of the target atom as seen from the reference frame of the projectile, B_p is the positive binding energy of the projectile, and B_t is the positive binding energy of the target.

The last term in the REC energy equation, $\vec{v} \cdot \vec{p}$, is the overlap of the projectile velocity and the momentum of the target electron. The target electrons have a non-zero velocity distribution which is described by the Compton profile $J(p_z)$ [38], where the beam direction is defined as the z-axis. The Compton profile represents the probability of finding the electron in a beamline projection p_z and results in broadening of the REC peak, especially in comparison to the characteristic x-ray emission lines. This can be seen clearly in the 297 MeV/u U^{92+}+Ar doubly-charge changed spectra from Bednarz *et al* [8] shown in Fig. 3, where the K-REC peak is broader than the characteristic uranium K-shell emission lines (labeled as Ly_α and Ly_β). The Compton profile grows in width with target atomic number Z and binding energy. Therefore capturing K- and L-shell electrons results in a broad emission peak.

The target electron binding energy is small compared to the kinetic energy of the electron in the projectile reference frame, making the approximation that the target electrons are quasi-free appropriate. In this context the REC process is identical to radiative recom-

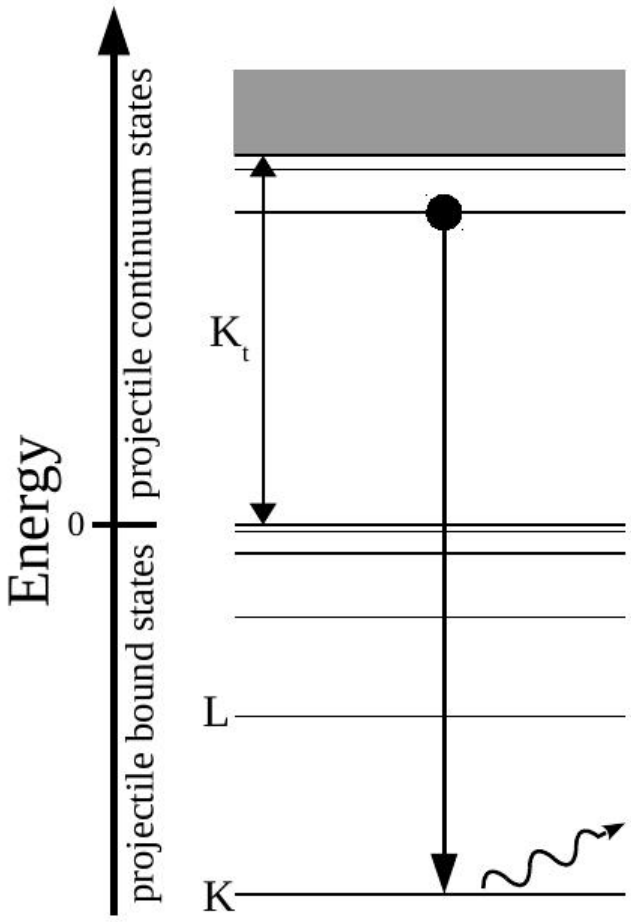

Figure 2: Radiative Electron Capture

bination (RR) and the principle of detailed balance can be applied. In this way REC can be treated as the time-inverse of PI theoretically. It should be noted the REC cross section scales as follows [39, 40]:

$$\sigma_{\mathrm{REC}} \propto \frac{Z_p^5 Z_t}{v_p^5} \tag{3}$$

The REC cross section therefore increases strongly with the atomic number Z_p and decreases as the velocity v_p of the projectile increases. Comparison of Eq. 1 and Eq. 3 shows that NREC decreases more strongly as v_p increases than does REC, but increases more strongly with Z_t. While the targets of interest in this work are low Z_t, REC will have a significant cross section and must be considered. It should also be noted that the differential cross section for σ_{REC} scales as $\sin^2\theta$ [27]; the cross section should therefore be largest at 90° to the beamline.

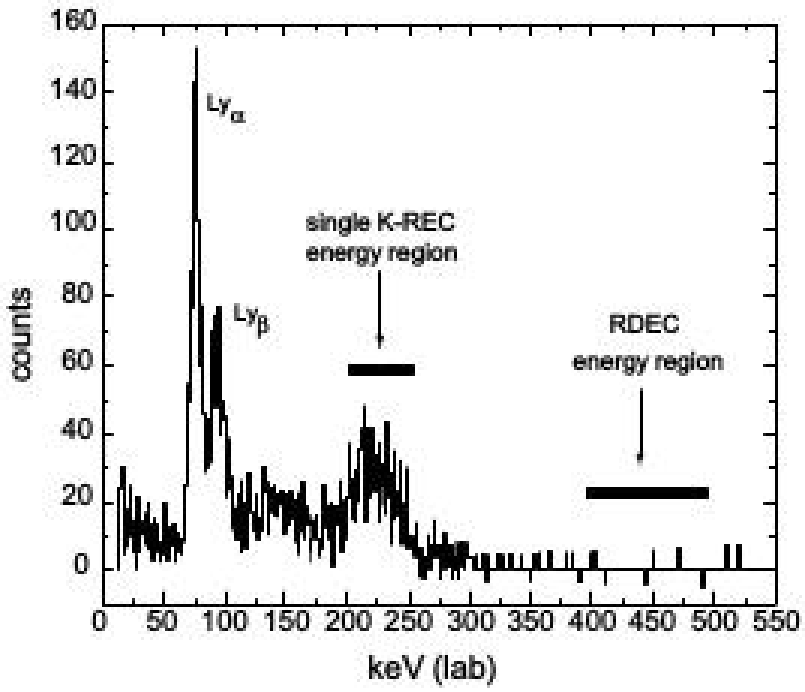

Figure 3: Doubly charge-changed x-ray spectrum from Bednarz *et al* [8].

Placing the x-ray detector perpendicular to the beamline was chosen for this reason and experimental simplicity. This angular factor integrated over spherical coordinates ($\frac{8\pi}{3}$) will appear in the REC cross section.

2.5 Radiative Double Electron Capture (RDEC)

The collision of an ion and an atom or molecule can result in the capture of one, two, or more electrons. The concept of two-electron capture with one-photon emission was introduced briefly in a conference abstract by Miraglia and Gravielle [6] in 1987 and will be referred to as radiative double electron capture (RDEC). More precisely, RDEC is a one-step process by which two target electrons are captured to the projectile ion with the simultaneous emission of a single photon. An example of this process is shown in Fig. 4. Analogous to DPI, for two electrons to be captured with the emission of a single photon, the electrons must interact in some way, i.e., via electron correlation. In a similar manner as REC, the released photon

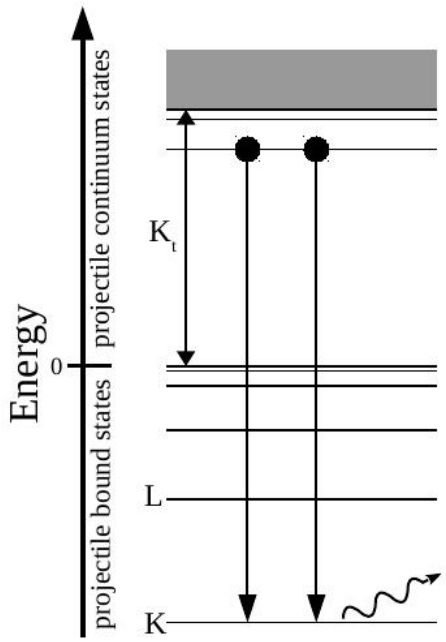

Figure 4: Radiative Double Electron Capture: Example shown is double electron capture from target bound KK state to projectile bound KK state with the emission of a single photon.

energy can be described in the following way:

$$E_{RDEC} = 2K_t + B_p^1 + B_p^2 - B_t^1 - B_t^2 + (\vec{v} \cdot \vec{p})^1 + (\vec{v} \cdot \vec{p})^2 \quad (4)$$

where the indices 1 and 2 represent the first and second captured electron. The RDEC energy can be approximated as twice the REC energy: $E_{REC} \approx 2E_{RDEC}$, thus giving a clear distinction in energy between the REC and RDEC processes. The presence of two Compton profiles in the energy equation means that the peak for any given RDEC transition will more broad than REC. RDEC is one of the two principal studies of this dissertation and therefore deserves a more thorough literature review than the other atomic collision processes mentioned previously.

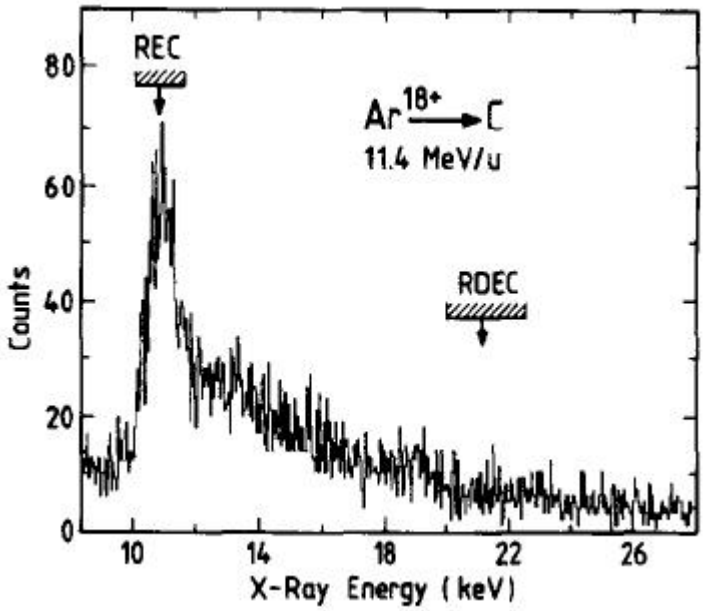

Figure 5: Doubly charge-changed x-ray spectrum from Warczak *et al* [7].

2.5.1 RDEC Experimental Review

The search for RDEC began with the first publication in 1995 by Warczak *et al* [7]. The experiment was performed at the Gesellschaft für Schwerionenforschung (Society for Heavy Ion Research) Helmholtz Centre for Heavy Ion Research, hereafter abbreviated as GSI, in Darmstadt, Germany, using the Universal Linear Accelerator. Fully-stripped argon ions (Ar^{18+}) were accelerated to 11.4 MeV/u and passed through a thin carbon foil. A typical doubly charge-changed x-ray spectrum for Ar^{18+}+C is shown in Fig. 5. The x-ray background is such that REC can clearly be seen, while RDEC cannot. This work reports an estimate for the upper limit for the total cross section of 5.2 mb for RDEC.

The search for RDEC continued in 2001 at the heavy ion storage ring (ESR) at GSI. The thought at the time was that high-energy, high-Z projectiles would register a significant number of RDEC events. The next attempt was performed with bare U^{92+} at 286 MeV/u on gaseous N_2 and Ar targets with densities ranging from $4.7 \cdot 10^{11} - 5.9 \cdot 10^{12}/\text{cm}^3$ [41]. REC and uncorrelated double capture (DREC) were measured successfully for both targets. Only a few photons with twice the energy of K-REC were registered throughout the U^{92+}+Ar

experiment. The authors assumed an isotropic distribution for RDEC and reported an estimated upper limit on the cross section of ∼100 mb. However, an isotropic distribution for RDEC is likely incorrect, given that REC has an angular distribution that behaves as $\sin^2\theta$.

Fully-stripped uranium is the heaviest bare ion currently possible. The beam energy was increased somewhat and the results of a new experiment were reported in 2003 from GSI for 297 U^{92+}+Ar [8], with the target density being about $5 \cdot 10^{12}/\text{cm}^3$. The x-ray spectrum for double charge exchange from this experiment can be seen in Fig. 3. The characteristic K-shell x rays can clearly be seen (labeled Ly_α and Ly_β), as well as the broad K-REC peak. However, in the RDEC energy region only a few counts are seen, if any. An estimated upper limit of ∼8 mb was reported for RDEC in U^{92+}+Ar. It should be noted that the angular distribution of REC was confirmed quite well in this work, as opposed to the previous Bednarz *et al* [8] work described above.

The unsuccessful experimental results reported above prompted a new line of thinking in the search for RDEC. Theoretical considerations mentioned in the next section, along with the pragmatic issue of available facilities, led to an RDEC investigation at WMU in 2009 using mid-Z, low-energy projectiles. The first successful observation of RDEC was reported by Simon *et al* [14] using 2.38 MeV/u fully-stripped oxygen (O^{8+}) projectile ions on a thin carbon foil target. The singly- and doubly-charge changed x-ray spectra can be seen in Fig. 6. RDEC peaks can be seen in both the single and double capture channels, and even more so in the single capture channel. This is due to the density of the target, so multiple collisions are likely producing RDEC in the single capture channel. Reported results are an RDEC to REC count ratio of 0.0092(6) and a differential RDEC cross section of 0.71(5) b/sr at 90° observation angle.

The results related above were then compared to Monte Carlo simulations in a 2011 publication [42]. The simulation considered capture only to the ground $1s^2$ and excited $1s^12s^2$ states, as these were the capture states reported in the experimental work [14]. The

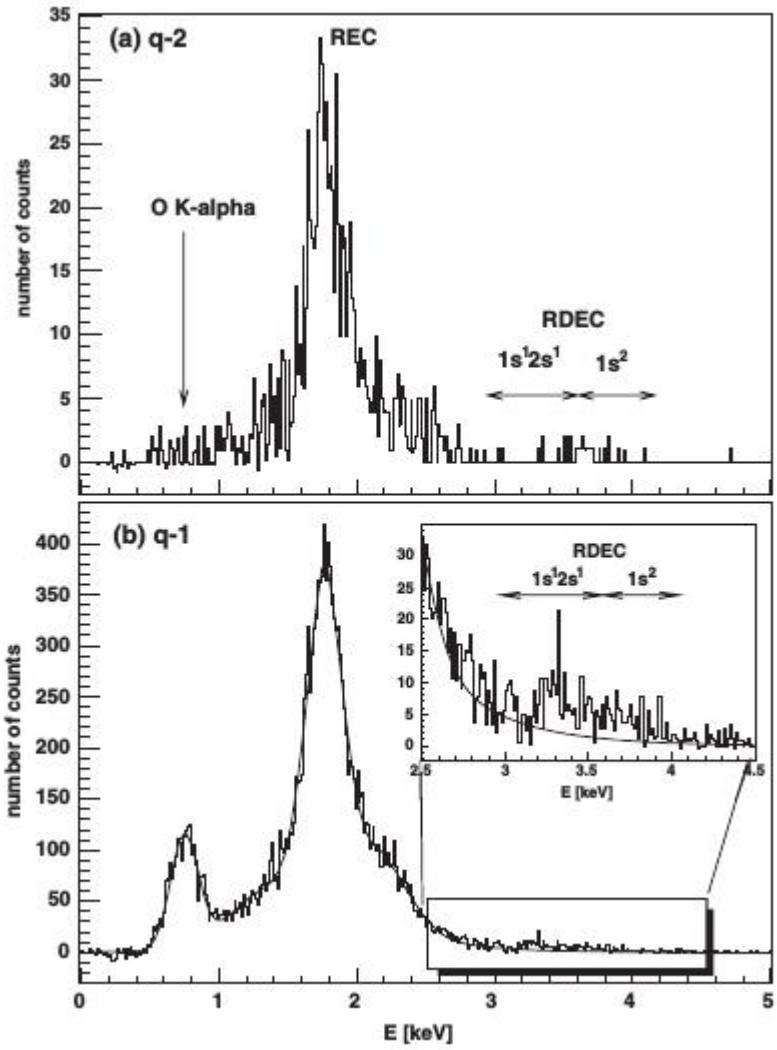

Figure 6: X-ray spectra from Simon *et al* [14].

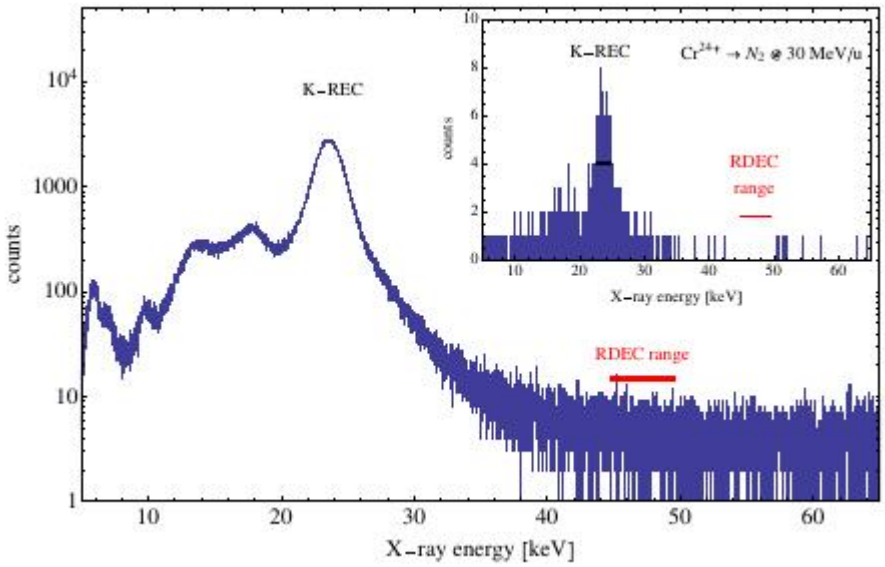

Figure 7: X-ray spectra from Winters *et al* [9].

cross section for capture to the excited state was assigned to be 70% that of the ground state, according to Ref. [13]. The angular distributions for DREC and RDEC were assumed to be the same as for REC. The simulations show quite well that DREC cannot account for the experimental results. Also the theory of Nefiodov [13] *et al* is insufficient to correctly predict the RDEC cross sections, most likely due to the quasi-free target electron assumption.

One more attempt was performed to observe RDEC using the ESR at GSI with results reported in 2013 using 30 MeV/u bare chromium (Cr^{24+}) projectile ions on a crossed N_2 gas jet [9]. The raw x-ray spectrum is shown in Fig. 7, with the doubly-charge changed spectra displayed in the inset. As in previous works at GSI, K-REC is clearly seen while sparse or no counts appear in the RDEC energy region. Unfortunately this experiment had little chance of success from the onset because of the prohibitively small amount of beamtime.

Following the success of Simon *et al* [14], a similar experiment was performed using 2.21 MeV/u fully-stripped fluorine (F^{9+}) on a thin carbon-foil target. The preliminary results were published in 2013 [43] along with the relevant background processes [44], with the final results published in 2016 [15]. The singly- and doubly-charge changed x-ray spectra from the latter are shown in Fig. 8. Qualitatively the results appear to show RDEC. A total differential

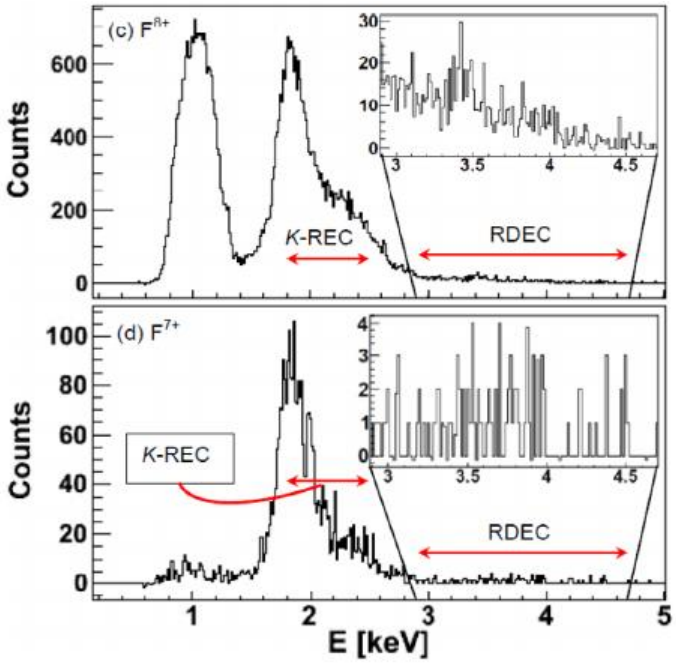

Figure 8: X-ray spectra from Elkafrawy *et al* [15].

RDEC cross section of 1.09(0.55) b/sr atom is reported in this work. However, the work is somewhat obfuscated due to impurity contaminations in the carbon foil, especially K and Ca.

The results at WMU for a carbon target are encouraging, but the presence of multiple-collision conditions and target contaminants remains an issue. Using diffuse gas targets solves both of these problems. The density of the gas can be tuned to ensure single-collision conditions and research-grade gas can be purchased commercially to remove worry of any contaminants. The major disadvantage of gas targets is the long beamtimes required to observe RDEC, namely ∼50-100 times as long as for the thin-foil carbon targets. Gas targets were chosen for the subsequent experiments performed at WMU.

2.5.2 RDEC Theoretical Review

Two-electron capture events have been of special interest to theorists over at least the past three decades. While most single-electron capture events are thought to be well-understood, the addition of another electron complicates the situation considerably. The works of

Yakhontov and Amusia [10, 11] in the 1990s are the first in-depth theoretical considerations of RDEC. Here, the lowest-order interelectron interaction is treated analytically by means of the Coulomb Green's function and the target atom is assumed to have quasi-free electrons so that RDEC can be considered the time-inverse of DPI. Ultimately, an upper limit for σ_{RDEC} is derived that is an order of magnitude larger than the measured value for the 295 MeV/u U^{92+}+C experiment [7] available at that time.

The work of Mikhailov *et al* [12], published in 2004, applied the theoretical method [12] for finding the cross section for double K-shell photoionization of an atom. In it the cross section was calculated for double electron capture to the K shell of a bare nucleus. The electrons were considered to be in the non-relativistic domain, meaning the Coulomb parameter is small ($\alpha Z \ll 1$, α being the fine structure constant). The leading terms in the αZ and $1/Z$ expansions can then be treated with perturbation theory with respect to the electron-electron interaction. The results were then compared to the experimental results available at the time. Their method worked quite well for light ions (within a factor of 2), but not nearly as well for heavy ions (worse than two orders of magnitude).

The work of Nefiodov *et al* [13], published in 2005, follows the work of Mikhailov *et al* and calculates the likelihood of RDEC by a bare, light nucleus and formation of the excited $1s2s\ ^1S$ state of the heliumlike ion. The dipole approximation is used in the treatment of the electron-photon interaction. It was shown that the RDEC cross section increases rapidly in the low-energy regime and that capture to the excited 2^1S state of heliumlike ions is much more likely than capture to the ground 1^1S state.

In 2006 Voitkov *et al* [45] considered the two-electron capture single-photon emission process in two ways. First the process was considered to be non-correlated, such that the two electrons are captured to the projectile independently via non-radiative and radiative channels. Correlated capture (RDEC) was then considered. Two conclusions were reached using a semi-classical, non-relativistic approach while employing various approximations along the way, including the Born and impulse approximations. First, the non-correlated capture

process has a maximum at the REC photon energy and is the main contributor to the two-electron capture processes. Second, the correlated capture process has a maximum at twice the REC energy and has a very small cross section. This, in principle, enables the separation of these processes in an experiment.

The work of Mikhailov *et al* was continued by Drukarev [46] in 2007, in which the high-energy nonrelativistic limit for double electron capture from a light target atom ($Z_t \ll Z$) to the K shell of a heavy, bare projectile nucleus ($Z \gg 1$) was considered. This limit implies that the velocity of the target v in the projectile rest frame is large compared to the velocities of the electrons in the ground state of the heavy nucleus ($v/c \gg \alpha Z$) and the energies of the colliding systems are nonrelativistic ($v \ll c$). It follows that $(\alpha Z)^2 \ll 1$. This enables the bound electrons to be described by nonrelativistic functions and the series expansion of αZ, of which only the lowest order is retained. RDEC cross sections are reported and they ultimately conclude that the cross section scales in a simple way: $\sigma_{\mathrm{RDEC}} \propto (\frac{Z}{c})^7$.

A more recent relativistic calculation was performed in 2011 by Chernovskaya *et al* [47]. Here, double electron capture to a bare nucleus is considered resulting in the emission of a single photon with the helium-like ion being in the ground state. Their evaluation was done within the framework of quantum electrodynamics and employed the line-profile approach (LPA). The LPA considers the non-resonant line profiles, such as RDEC, to behave in the same manner as the natural resonant line profiles. In this model, the momenta of both captured electrons were taken to be identical, corresponding to the experimental situation. Two models were developed in this work. The first model sets the electron density as homogeneous in the target atom (model A). The second model sets the target K-shell electron density as homogeneous and only accounts for its contribution to the process (model K). Model A under estimates the cross sections for RDEC in comparison to theory for both light [14] and heavy [8] ions, although the reliability of the latter experimental results are in question. Model K grossly underestimates the experimental cross sections by two orders of magnitude or more for light and heavy ions. Surprisingly, model A greatly overestimates

the cross section for mid-Z (18) [7] projectiles, while model K is comparable. They conclude that for the quasi-free electron model to be appropriate, the target atoms being much lighter than the bare nucleus is preferable.

The work of Chernovskaya (now Mistonova) *et al* [47] was extended in 2013 [48]. This work considers ions with charge $8 \leq Z \leq 92$ and the electrons captured to bare nuclei. It is assumed that the captured electrons have the same energy, are non-interacting in the initial state, and are captured to the $1s1s$ state (K shell). The two models (A and K) previously mentioned were again used. In this work, σ_{RDEC} was calculated for both models and compared to the experimental values available at the publication date. Both models tend to underestimate the experimental values for carbon targets [14, 15]. It is concluded that the RDEC cross section depends on the electron density, explaining the strong dependence of σ_{RDEC} on the target.

2.6 REC and RDEC Energies

In order to properly analyze the experimental spectra described later in Section 4 the photon energies for REC and RDEC must be calculated. Also of consequence in those calculations are the Compton profiles of the transitions.

2.6.1 REC and RDEC Transition Energies

To find the REC and RDEC transitions energies several values must be known or calculated. For the purposes of this dissertation 40 MeV F^{9+} and F^{8+} + N_2 and Ne will be considered. The kinetic energy K_t is therefore:

$$K_t(40\ \mathrm{MeV}) = \frac{40E6}{19*1836} = 1146.7\ \mathrm{eV}$$

All binding energies are taken to be positive. The binding energies of the projectile are [49]:

$$B_p^1(F^{9+}) = 1103.1\ \mathrm{eV} \qquad B_p^1(F^{8+}) = 953.9\ \mathrm{eV}\ \text{(capture to K shell)}$$

For capture to the L shell ($2s^1$ state) of F^{8+}, consider $Z_{\mathrm{eff}}=8$, so:

$$B_p^2(F_{2s^1}^{8+})=\frac{(Z_{Eff}=8)^2*13.6}{(n=2)^2}=217.6 \text{ eV}$$

The binding energy of a K-shell electron in neutral N_2 and Ne is [50]:

$$B_t(N_2)=409.9 \text{ eV} \qquad B_t(Ne)=870.2 \text{ eV}$$

For capture to the projectile L shell in bare fluorine (only appropriate for REC) $Z_{eff}=9$, so:

$$B_p(L)=\frac{(Z_{Eff}=9)^2*13.6}{(n=2)^2}=275.4 \text{ eV}$$

Electrons captured from the target L (valence) shell are considered to be quasi-free with binding energies equal to about zero and are referred to as V (for valence) electrons. Given these definitions, the REC and RDEC transition energies are given in Tables 1 and 2. The V→L REC transitions for both targets lie under the large peak attributed to characteristic target (for Ne) and projectile ion x rays, as discussed later in Section 4. The REC and RDEC transitions for Ne unfortuntaly overlap, a problem discussed in Sections 4 and 5. For the F^{8+} projectiles, all transitions are taken to be 50 eV lower.

Table 1: REC transition energies (in keV) for 40 MeV F^{9+} projectiles. V refers to valence (quasi-free) electrons.

REC Transition	N_2	Ne
V→L	1.42	1.42
K→K	1.84	1.38
V→K	2.25	2.25

Table 2: RDEC transition energies (in keV) for 40 MeV F^{9+} projectiles. V refers to valence (quasi-free) electrons.

RDEC Transition	N_2	Ne
KK→KL	2.79	1.87
VK→KL	3.20	2.74
KK→KK	3.53	2.61
VV→KL	3.61	3.61
VK→KK	3.94	3.48
VV→KK	4.35	4.35

2.6.2 Compton Profiles

The electron captured to the projectile has an average momentum distribution in its initial bound state that differs between shells and subshells within the neutral target. This momentum vector $\vec{p}$ does not necessarily align the with velocity vector $\vec{v}$ of the projectile. The emission due to a captured electron has a natural linewidth that is dominated by the

term(s) $\vec{v} \cdot \vec{p}$ in Eqs. 2 and 4, called the Compton profile. The calculation of the general Compton profiles for N_2 and Ne was done analytically using the impulse-approximation for nonrelativistic one-electron wavefunctions [38]. In that work, the Compton profile $J_{nl}(Q)$ is defined as:

$$J_{nl}(Q) = \frac{1}{2} \int_Q^\infty |\chi_{nl}(p)|^2 p dp$$

with normalization factor:

$$2 \int_0^\infty J_{nl}(Q) dQ = 1$$

where n and l are the principal and orbital quantum numbers, Q is the projection of the momentum transfer k on the original electron momentum $\vec{p}$ before the collision (so $Q = -\frac{\vec{k} \cdot \vec{p}}{k}$), and $\chi_{nl}(p)$ is the Fourier transform of the spatial wavefunction.

In the work of Biggs *et al.* [38], Q is tabulated in units of $me^2/\hbar$, the average electron momentum in the ground state of hydrogen. Taking the ground state of hydrogen to be 13.6 eV, the mass of an electron, and $E = \frac{1}{2}mv^2$ one arrives at $v_e = 2.19 * 10^6 \ \frac{m}{s}$ and consequently $p_e = 1.99 * 10^{-24} \ kg\frac{m}{s}$. Taking the energy of the projectile beam as 40 MeV, the mass of the projectile as $(19) * 938 \ \frac{MeV}{c^2}$ and $E = \frac{1}{2}mv^2$ leads to a beam velocity of $v_b = 2.00 * 10^7 \ \frac{m}{s}$. Therefore the term $\vec{v_b} \cdot \vec{p_e} = 3.98 * 10^{-17}$ J $= 248$ eV is multiplied by Q in the tables of Biggs *et al.* [38] to obtain the Compton profiles. Examples of these profiles are shown in Fig. 9 for a) N_2 and b) Ne.

The more tightly bound electrons ($1s^2$) have a significantly broader Compton profile than do the more weakly-bound outershell electrons, owing to their higher average momentum. Due to this same effect, higher-Z species also have broader profiles than their lighter cousins.

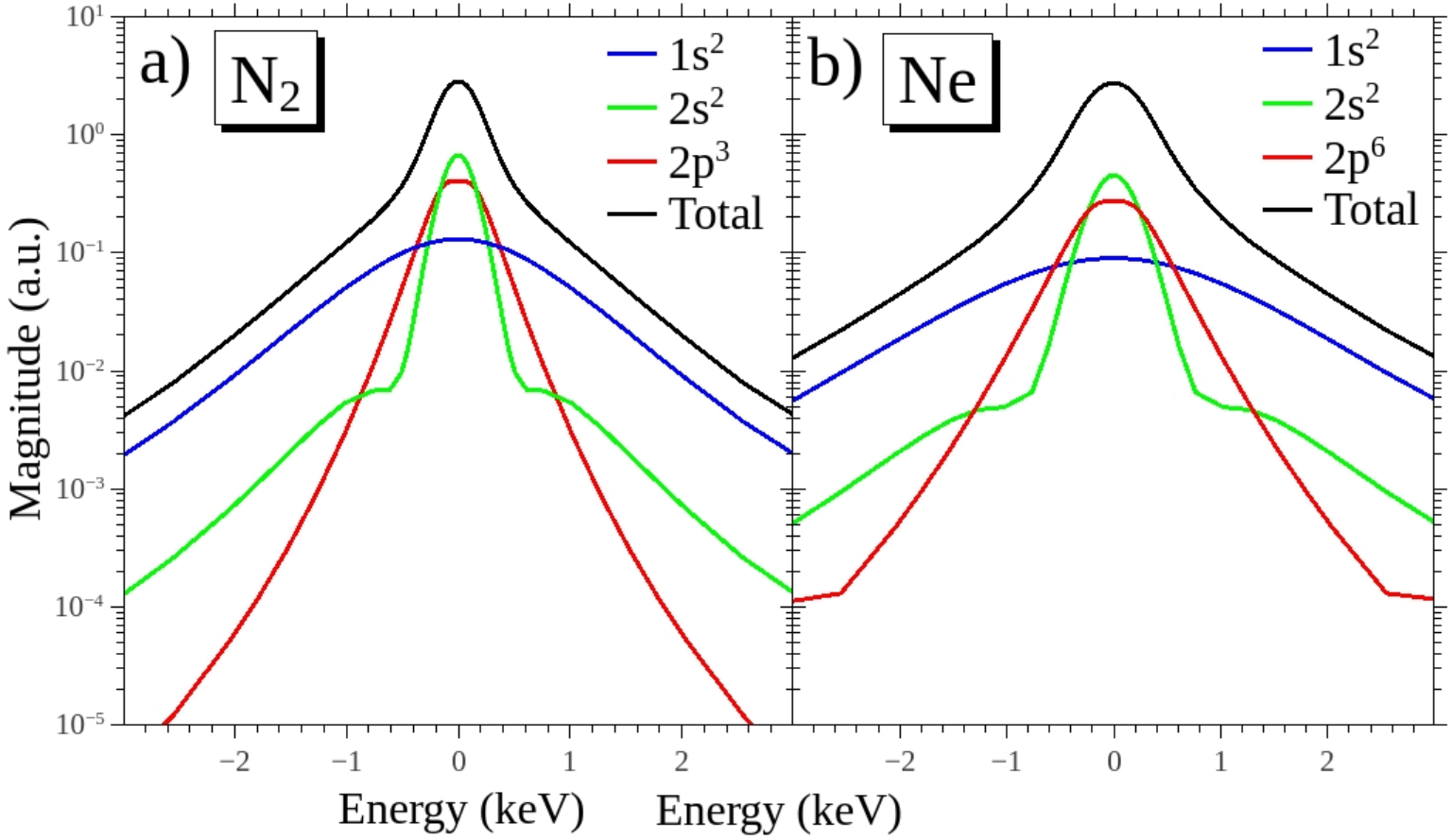

Figure 9: Compton profiles for a) N_2 and b) Ne calculated from Ref. [38].

3 Experimental Configuration

3.1 Tandem Van de Graaff Accelerator Facility at Western Michigan University

3.1.1 Source of Negative Ions

The work for this dissertation was performed using the tandem Van de Graaff accelerator facility at Western Michigan University (WMU). Negative ions must be input to the accelerator so that they are attracted to the positive terminal. A source of negative ions by cesium sputtering (SNICS) has been available since at least the 1970s [51, 52]. The SNICS at WMU is a commercial device from the National Electrostatics Corporation that creates negative ions from a solid source through collisions with Cs^+, shown schematically in Fig. 10. The SNICS has an oven, generally kept at 140 ^{0}C, that creates cesium vapor. The vapor travels from the oven to an enclosed area containing the water-cooled cathode and the heated ionizing surface. The cathode is filled with solid material comprised of the ion of choice, in this case, powder form LiF and a small amount of silver to aide in ion production, and set at a high negative voltage. The ionizing surface is heated by passing a controllable current through it.

When the cesium vapor touches the heated surface, i.e. ionizer, some of it becomes ionized as Cs^+. The Cs^+ is drawn towards and focused onto the cathode by electrodes (not pictured). The accelerated cesium then sputters negative ions through a condensed cesium surface on the cathode. Some materials preferentially sputter negative ions, while others sputter neutral or positive ions. Fluorine is a species that sputters negative ions and can be used for a strong outgoing ion beam. The negative potential of the cathode and the positive potential of extractor plates accelerate the negative ions out of the SNICS towards the accelerator terminal. The entire cesium vapor and ion production areas must necessarily be kept at high vacuum.

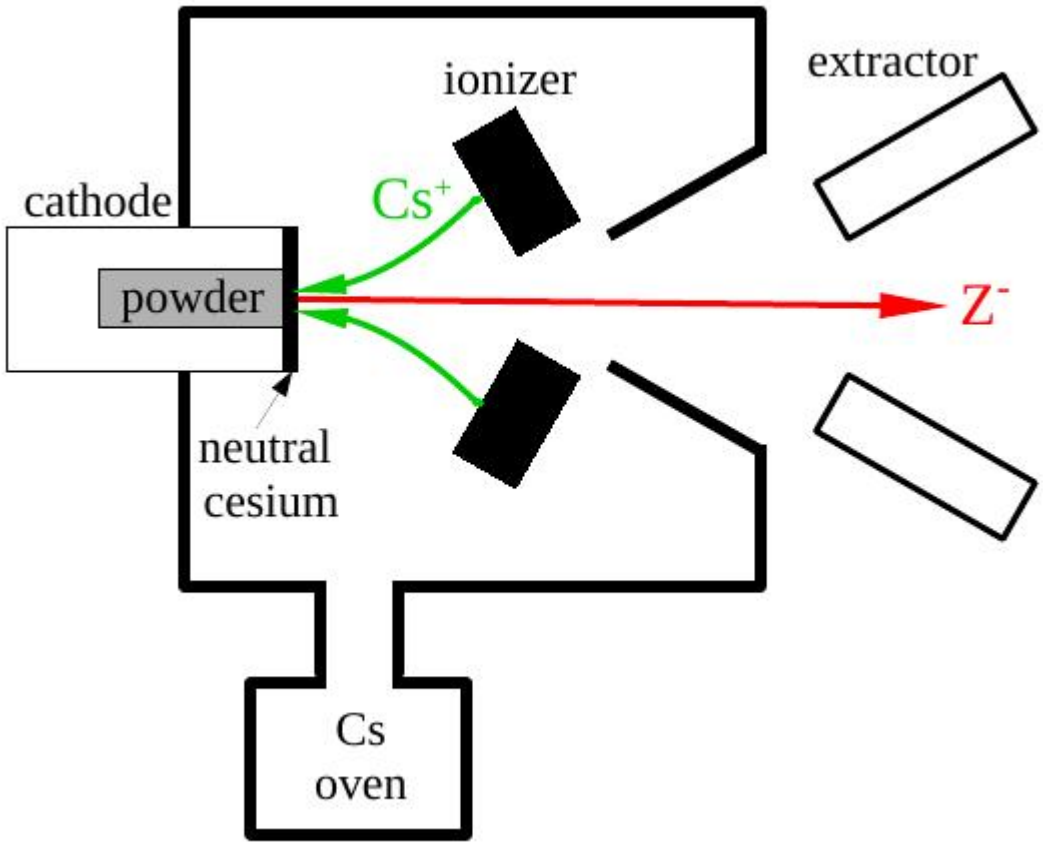

Figure 10: Source of Negative Ions by Cesium Sputtering (SNICS) A heated surface (ionizer) creates Cs^+ which are focused onto the cathode by electrodes (not pictured). The negative ions (Z^-) are then sputtered from the cathode, extracted, and sent on to the accelerator.

3.1.2 Accelerator

The accelerator at WMU is essentially two large Van de Graaff generators [53] in tandem. A schematic of the accelerator is shown in Fig. 11. There are two chains within the accelerator tank composed of conducting elements separated by a dielectric material (in this case stainless steel and plastic) running over a pair of rollers. One roller is inside a hollow, metal shell called the terminal and is connected to the terminal by an electrode. The lower roller is connected to a high-voltage DC source, in this case capable of 50 kV, via another electrode. As the chain moves it deposits positive charges on the upper electrode, and in turn on to the terminal. The voltage on the lower electrode is adjusted high enough that the rate of discharging and charging of the chain comes to equilibrium.

The accelerator tube is under vacuum ($10^{-7} - 10^{-8}$ Torr), while the tank of the accelerator is filled with mostly gaseous N_2 and CO_2, plus a small amount of SF_6, to insulate the volume surrounding the terminal, chains, and electrostatic plates used to charge the electrode. This helps to prevent spontaneous discharge of the terminal to the enclosing tank. Small needles (corona points) on a movable arm are positioned close to, but not touching, the terminal. The corona points serve to remove excess charge and stabilize the terminal voltage. Moving the corona points farther or closer to the terminal removes charge more slowly or quickly, respectively, aiding in stabilizing the terminal voltage. The WMU accelerator is nominally capable of creating an electrostatic potential of 6 MV, but electrostatic accelerators exist capable of up to 25 MV [54].

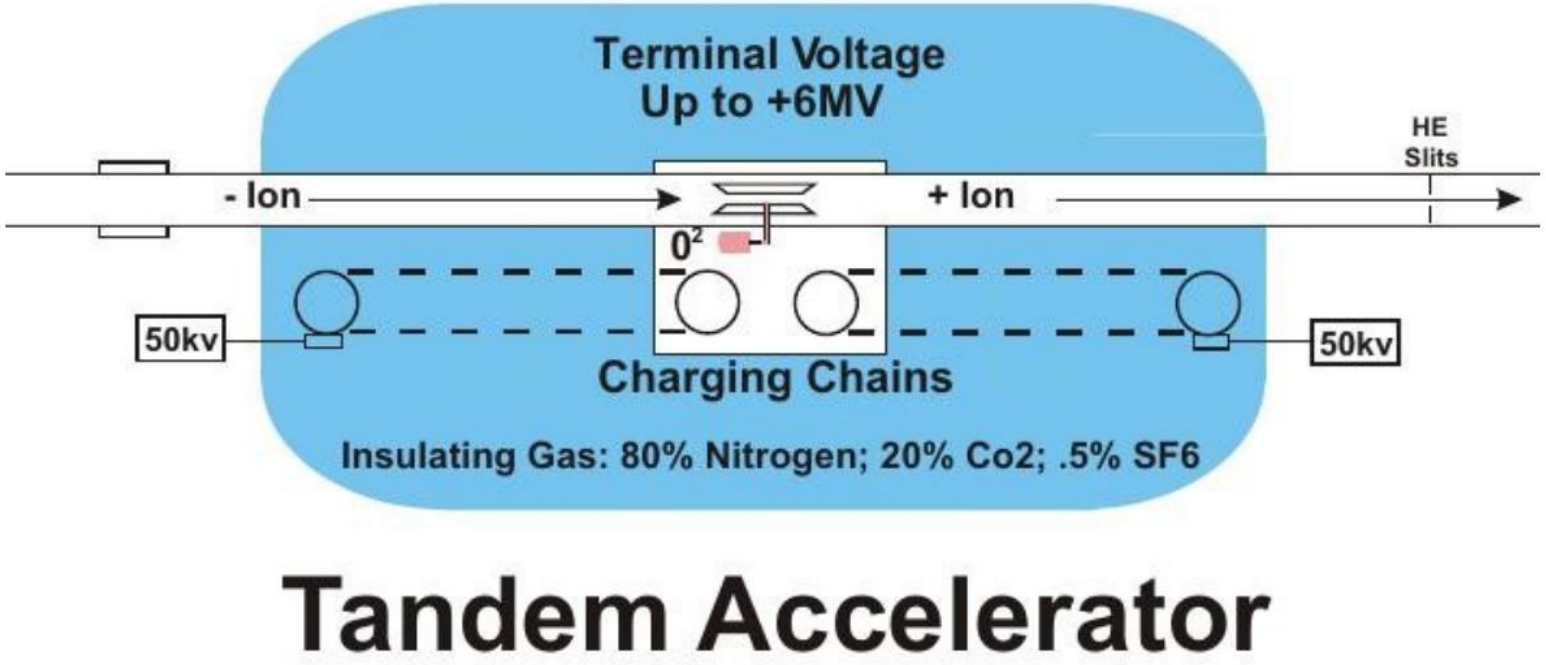

Figure 11: Schematic of tandem Van de Graaff accelerator at WMU. [55].

3.1.3 Accelerator Facility

The large positive potential of the terminal attracts the initially negative ions. Stripping gas (generally O_2) in the terminal region is then used to remove electrons from the ions by collision, creating positive ions. These ions are then accelerated out of the accelerator by the positive terminal. The number of electrons removed from the ion overall is $q + 1$ and the ions therefore receive $(q + 1)V$ in kinetic energy, where V is the terminal voltage and q is the outgoing charge state.

A 90° analyzing magnet is used to select ions with the desired energy and charge state, in this case F^{7+}. The stripping gas in the accelerator is not able to strip away the most tightly bound K-shell electrons of F^{7+} ions, of which there are two. So, when required, the ions are post-stripped to F^{8+} or F^{9+} by a thin carbon foil. The energy decrease of the beam from passing through the foil is negligible. The ion beam is then deflected into the target beamline, as shown in Fig. 12.

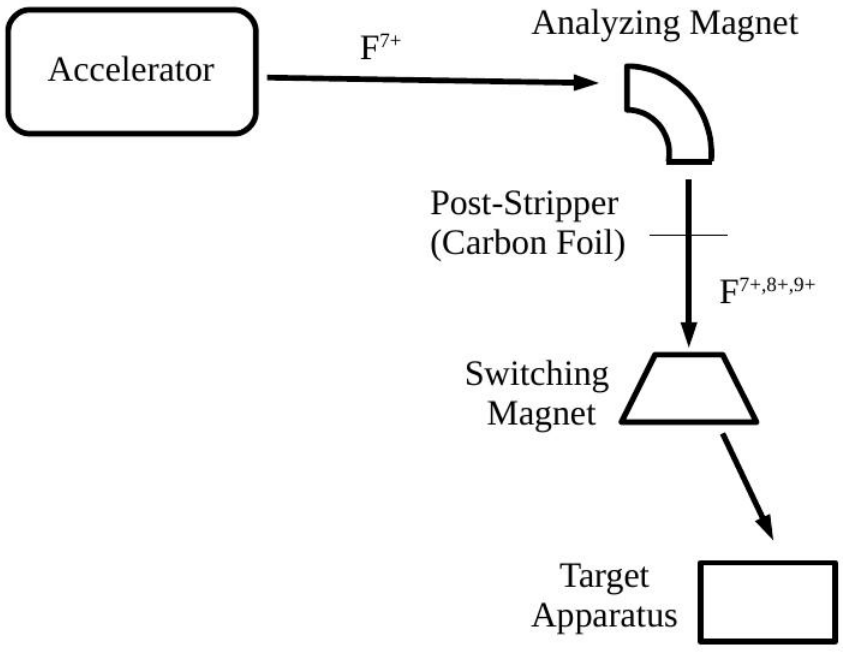

Figure 12: Accelerator Facility Setup

The incoming ion beam is collimated by adjustable apertures before entering the interaction region, which is shown in Fig. 13. The collision chamber is a differentially-pumped gas cell 3.65 cm long with entrance and exit aperture diameters of ∼3 mm. The target gas pressure is measured using a capacitance manometer in a voltage feedback loop to control a valve on the chamber, setting the pressure in the cell to remain in the single-collision regime where charge exchange is less than 5%. A Canberra model Si(Li) x-ray detector is placed at 90^o to the beamline. This detector provides a detection efficiency of over 90% above 2 keV and an actual energy resolution (FWHM) of 157 eV for the Mn K_α lines (∼5.9 keV) obtained from a ^{55}Fe source. The x-ray detector has an effective area of about 60 mm^2, with a beamline-to-crystal distance of ∼17 mm.

After passing through the collision chamber, the ion beam is charge-state analyzed using a dipole magnet. The primary ion beam, measured with a Keithley electrometer, is then collected by a Faraday cup biased to -200 V to suppress ejected electrons, digitized, and integrated to give the number of incident particles. The singly and doubly charge-changed beam components are collected with silicon surface-barrier particle detectors that have an efficiency of unity.

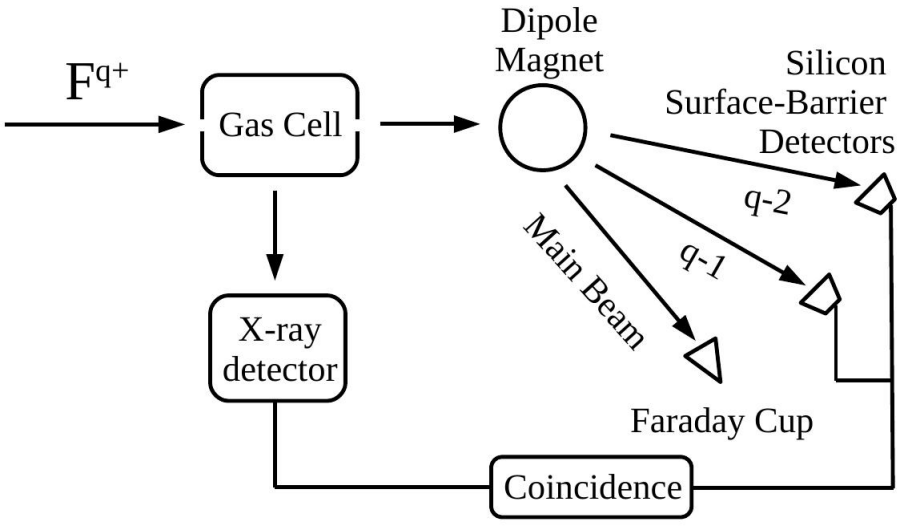

Figure 13: Target Room Setup

3.2 Data Acquisition System

The x-ray and particle data were collected using an event-mode data acquisition system following their observation by separate detectors that produce linear analog signals requiring appropriate conditioning before the computer can record final analog or logic (digital) signals. Linear signals have their relative amplitude preserved by electronic modules while logic pulses have a fixed amplitude. There are two types of logic signals shown in Fig. 14 that pertain directly to the experimental setup used here: transistor-transistor-logic (TTL) and Nuclear Instrumentation Module (NIM). Both of these have two possible states: Logic 0 and Logic 1. TTL signals have Logic 1 positive square-waves typically 5 V in amplitude and 0.5 μs in width, and are therefore considered slow logic signals, while Logic 0 has amplitude 0 V. NIM signals have negative Logic 1 typically -1.0 V with widths on the order of tens of ns, and are therefore considered fast logic signals, with Logic 0 having an amplitude of 0 V.

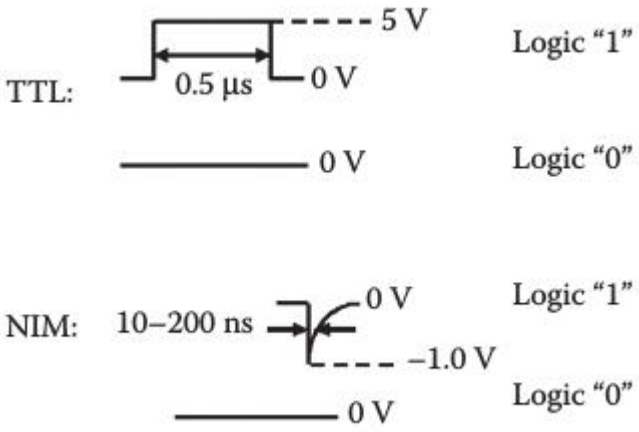

Figure 14: Examples of logic pulses. Image taken from Ref. [56].

It is appropriate here to define certain electronic modules that were used in the execution of the experiment and make up the Coincidence Circuit and Beam Current Integration setup.

Pre-amplifier A pre-amplifier (henceforth called PRE-AMP) is a linear device used to increase the pulse signal created by a detector. The PRE-AMP is generally located physically close to the detector, sometimes even being integrated into the detector, to minimize signal attenuation and electronic noise. The PRE-AMP may also do some signal conditioning that, along with amplification, make the signal appropriate for subsequent amplification.

Spectroscopy (Slow) Amplifier A spectroscopy amplifier (henceforth called SPEC AMP) is a linear device that increases the detector pulse signal and modifies the pulse shape. The SPEC AMP input pulse magnitude is proportional to its output (generally 0-10 V) with a pulse width on the order of μs to maximize energy resolution. The resulting analog signal(s) created by the SPEC AMP can be converted directly to digital signals for energy analysis or used in subsequent timing schemes.

Timing Filter (Fast) Amplifier A timing filter amplifier (henceforth called TFA) is a linear device used to amplify and shape an input signal in similar fashion to a SPEC AMP, but generally with a faster output width and a lower output magnitude (0-4 V). Generally, a TFA produces negative output signals and is used to condition a signal for input into a discriminator and subsequent conversion to a logic signal. The output pulses generally have widths less than 200 ns and can be positive or negative to match the requirements of the subsequent discriminator.

Discriminators Discriminators are devices that allow input pulses with amplitudes (voltages) greater than a certain set value to pass through the device while rejecting signals below the threshold. The point in time relative to the input signal that the device produces an output differs between types of discriminators. A leading edge discriminator rejects signals

with amplitudes below the voltage threshold as measured on the leading edge of the linear input. A constant fraction discriminator (henceforth called CFD) is essentially a leading edge discriminator that is triggered at a fixed time after the leading edge of the input pulse reaches a constant fraction of the original input pulse height. The CFD is therefore more appropriate for fast signals that may contain large amounts of electronic noise. The CFD generally has both TTL and NIM logic outputs. A single channel analyzer (henceforth called an SCA) is a discriminator that rejects signals both above and below separate thresholds with a logic output. The SCA is therefore a single-channel analog-to-digital converter. A multi-channel analyzer is another type of analog-to-digital converter that can count pulses based on their amplitudes or counts the number of pulses within a given time period.

Gate and Delay Generators A gate delay generator (henceforth called GATE/DELAY GEN) is a device that creates a logic (gate) signal after delaying the signal for a certain length of time, typically less than 1 ms. The time delay is usually adjustable by the width of an output pulse used for the accurate setting of the delay. In general, a gate signal is used to initiate or inhibit other electronic modules.

Linear Gate Stretcher A linear gate stretcher (henceforth called LGS) is a device that accepts linear signals and increases the width of those pulses by stretching the peak at its constant amplitude for a required length of time, typically up to $\sim$5 μsec. The device may or may not be gated by an external source. The gate may operate in coincidence or anti-coincidence mode, where an output is generated when the external gate is or is not present, respectively. Any pulse shaping retains the input pulse amplitude.

Logic Fan A logic fan-in/fan-put (henceforth called a FIFO) is a device capable of converting a single logic input to multiple logic outputs, or vice-versa. In the former case, the module essentially acts as an AND logic output. If multiple inputs are used and they all occur within the signal processing time of the module, the input essentially behaves as an

OR logic input. The signal is not purposefully conditioned or delayed with this module.

Level Adapter A level adapter is a device that converts one type of logic signal to another. This is generally done with an input of a NIM, inverted NIM (N$\bar{\text{I}}$M), TTL, or inverted TTL (T$\bar{\text{T}}$L) signal and an output of one or more of the types mentioned. The signal is not purposefully conditioned or delayed with this module.

Time-to-amplitude Converter A time-to-amplitude converter (henceforth called TAC) is a device that converts the actual time difference between a START input logic signal and a STOP input logic signal to an analog output pulse with amplitude proportional to that time difference with a typical amplitude of 10 V. The maximum time difference between the START and STOP signals can generally be chosen by the user.

Analog-to-digital Converter An analog-to-digital converter (henceforth called ADC) is a device that represents a voltage amplitude as an integer number. These are commonly used in conjunction with TACs or SPEC AMPs to convert the outputs of these devices to an integer number that a computer can understand. This integer is termed channel number and can vary depending on the units used and the desired resolution. In this experiment the ADC channel range is $2^{12} = 4096$.

Additional Electronics Certain other electronic modules, devices, and terms were used in the execution of this experiment. Several COUNTER/TIMER modules were used to measure elapsed time to 0.1 s precision and/or count the number of TTL or NIM signals input to them. When a gate signal prompts the processing of a signal by a module, that module is said to be triggered. A signal that initiates data processing by an ADC or computer is termed the STROBE. A MASTER module is initiated manually and causes its associated SLAVE modules to perform their intended functions. A Faraday cup is a metal cup that collects charged particles in vacuum where the product current can be measured and used to

determine the number of incident particles. A digital current integrator or current digitizer is an electronic module that accurately measures a direct current or the average value of pulse currents by creating a single output pulse for a user-adjustable amount of input charge (10^{-8} C here). Other electronics will be defined as appropriate.

3.2.1 Coincidence Circuits

The modules mentioned can be used in conjunction with each other to condition signals coming from the detectors for processing in coincidence circuits or by a computer. Ultimately, coincidences were assigned between the collected x rays and charge-changed particles. The schematic for the electronics is shown in Fig. 15.

The signal from the x-ray detector was passed through an integrated PRE-AMP and split to separate modules. One signal was sent to two TFAs in series to condition the so-called FAST signal before being passed to a CFD. After discrimination an outgoing positive TTL signal was used as a gate signal for an LGS module after passing through an SCA and an outgoing negative NIM signal was split by a FIFO for use as a START signal for the TACs. The other signal from the PRE-AMP was sent into a SPEC AMP with unipolar and bipolar outputs. The unipolar signal was split and one signal was sent through the LGS gated by the fast signal output of the TFA and on to the ADC as the so-called FAST signal and the other signal was sent through an ungated LGS and on to the ADC as the so-called SLOW signal. The bipolar signal was sent through an SCA to produce a strobe for the computer system as to when an event should be counted. This signal was split by the FIFO, with one output signal passed through a GATE/DELAY GEN that was used as a strobe for the ADC. That signal was gated by a signal from the MASTER TIMER and subsequent level adapter so that the ADC would be strobed only when data collection was taking place. The other outgoing FIFO signal also passed through a GATE/DELAY GEN before being used as a strobe for the data collection computer.

The signals from the q-1 and q-2 particle detectors were conditioned by PRE-AMPs and

TFAs before being delayed approximately 2 μs by a length of physical cable, sent through the CFD to eliminate electronic noise, and sent on to the TAC as the STOP signal. These particles were selected as the STOP signal to minimize electronic noise in the output of the TAC as there are many times more particle events than x rays. In principle the START and STOP could be reversed. The CFD also sent negative signals to COUNTERs slaved to the MASTER TIMER to register the number of charge-changed particles. The output of the q-1 and q-2 TACs were then passed on to the ADC. All input signals to the ADC were converted by the module and passed on to the computer. Examples of all mentioned spectra are shown in Section 4.

3.2.2 Beam Current Integration

The beam current integration (BCI) schematic is shown in the left inset of Fig. 15. The primary ion beam was collected by the Faraday cup which was biased to -200 V to suppress electrons ejected from the cup by the impinging ion beam which would give a falsely high current. The current from the cup was collected by a Keithley electrometer, which is a device capable of measuring ultra-high resistances and ultra-low currents. The full scale output of the electrometer is 2 V at all user-selected settings of the scale. The output of the electrometer was passed across a 1 mega-ohm resistor (denoted as Ω in Fig. 15) and on to the current digitizer set to 10^{-8} $\frac{\mathrm{C}}{\mathrm{pulse}}$ and finally to a COUNTER. The COUNTER is slaved to the MASTER TIMER to begin counting when data collection begins. The number of pulses registered by the COUNTER is termed the BCI, which stands for beam current integration. Noting that $\mathrm{I} = \frac{\mathrm{V}}{\mathrm{R}}$ $[\frac{\mathrm{C}}{\mathrm{s}}]$, the total number of incident ions collected by the Faraday cup was calculated as follows:

$$\mathrm{N_{ions}} = \mathrm{BCI} \ \cdot 10^{-8} \ \frac{\mathrm{C}}{\mathrm{pulse}} \cdot \frac{(\mathrm{Keithley\ \ full\ \ scale})\ \frac{\mathrm{C}}{\mathrm{s}}}{\mathrm{Q} \cdot \mathrm{e} \cdot \frac{2\ \mathrm{V}}{1*10^{6}\ \ \Omega}}$$

where Q is the ion charge state and e is the charge of an elementary particle ($1.60 * 10^{-19}$ C).

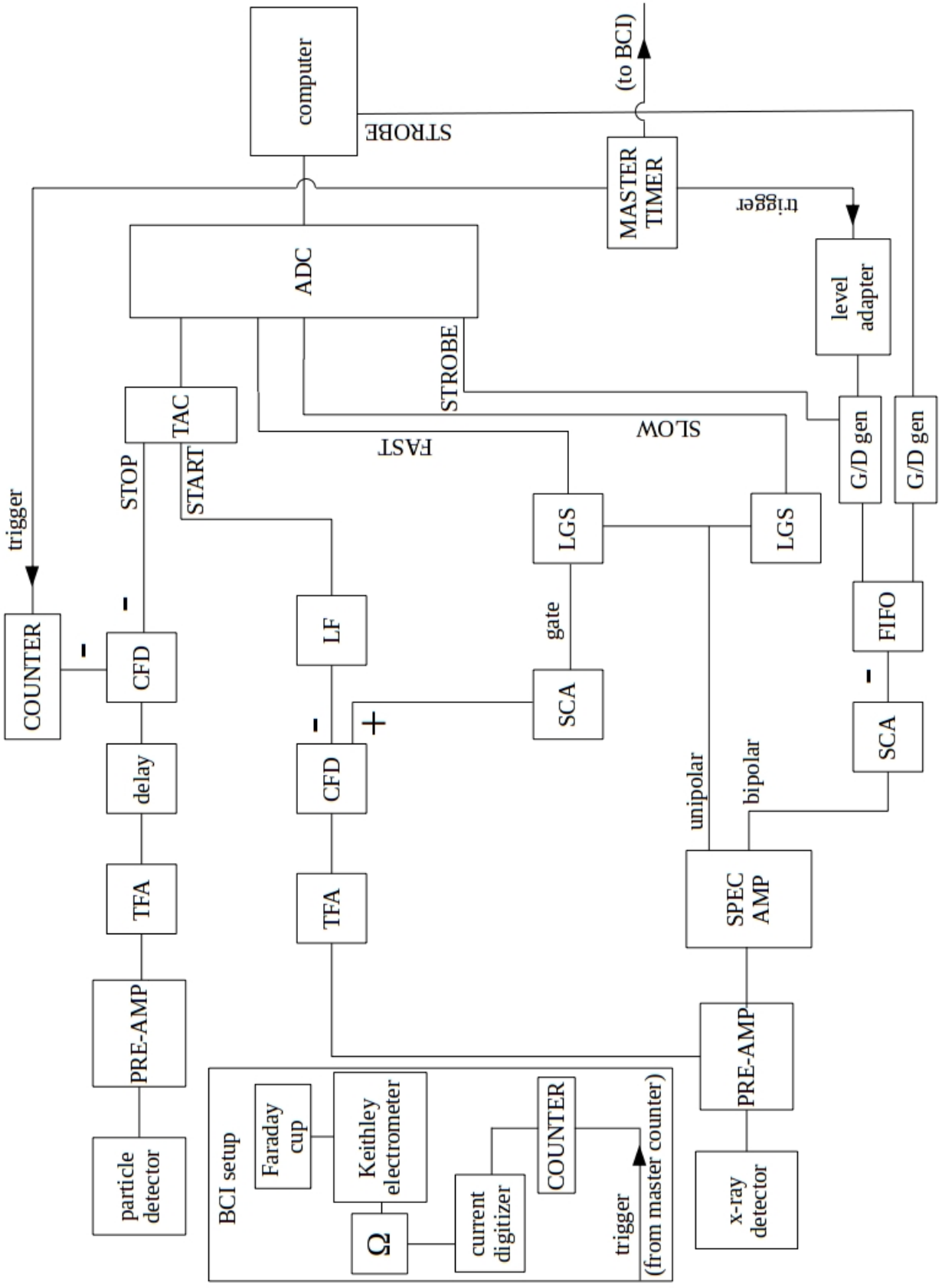

Figure 15: Schematic of electronics for recording coincidence data.

4 Data Analysis

Described in this Section is the analysis of data collected for F^{9+} and F^{8+} projectiles colliding with the target Ne gas. The raw data were collected by three separate detectors, as described in Section 3. The data were collected by the NSCLDAQ software and the subsequent sorting and preliminary data analysis was performed using the SpecTCL program [57]. Sorting algorithms described below were used to assign emitted x rays to their respective charge-changed particles, or vice-versa. REC and RDEC differential cross sections for $F^{9+,8+}$ were determined; however, the RDEC cross sections do not include the KK$\rightarrow$ transition, as this lies under the K REC peak. The REC cross section is further complicated by the impossibility of separating all of the REC (largely those due to L REC) events from the F K x rays.

The energy calibration for all spectra was performed using the Mn K_α and K_β lines from a standard ^{55}Fe source, as well as the hydrogen-like 1s-2p transition of fluorine [58]. The total number of incident particles for F^{9+} and F^{8+} were both $\sim$1.00x10^{12}. Runs were performed without target gas to ensure that the events of interest were not occurring falsely. Count rates from the BCI setup without the beam present were recorded to account for the dark current in the electronics to ensure the correct number of incident particles was used.

4.1 Raw Spectra

The x-ray signals generated from the SPEC AMP (the so-called SLOW x-ray signals) were used to strobe the ADC and data acquisition computer and for input into an LGS gated on the so-called FAST x-ray signals to ultimately create the final FAST spectra. The SLOW spectrum was also recorded to determine if some x-ray counts were "lost" and not recorded in the FAST spectrum. This turned out to be true only for the low energies in the region of the F x rays. Examples of collected SLOW and FAST x-ray spectra are shown in Fig. 16 a and FIg. 16 b.

Most prominent in the spectra are the projectile F K-shell x-rays. The REC events occur

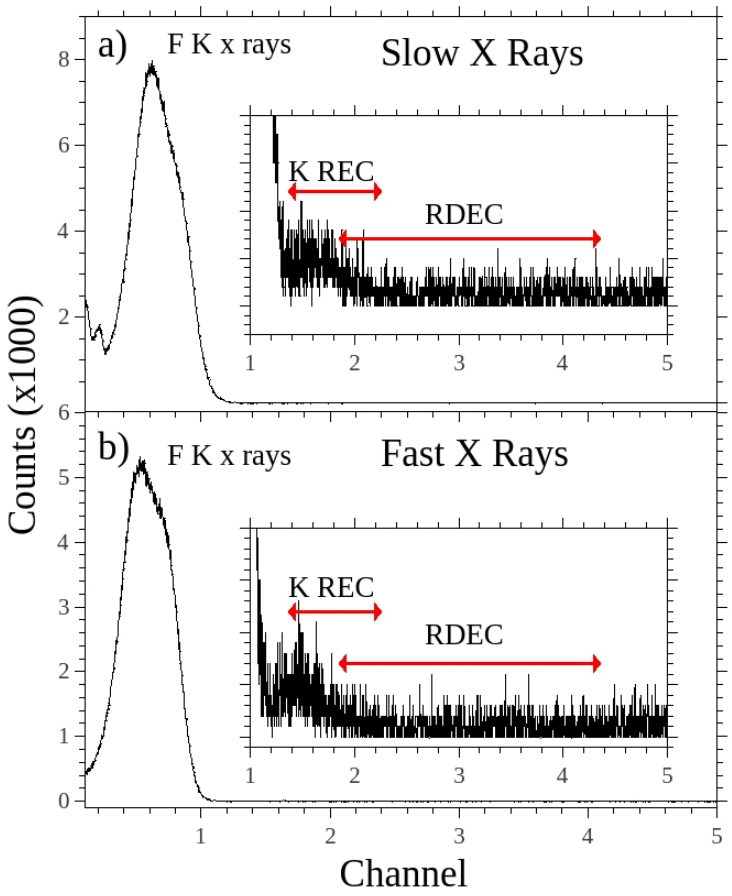

Figure 16: Examples of a) SLOW and b) FAST x-ray spectra for 2.11 MeV/u F^{9+}+Ne (15 mTorr).

on the high-energy side of this peak. The rest of the spectrum appears as background even though the RDEC events lie in the region indicated. Shown in both insets are the K REC and RDEC energy regions. REC to the L shell of the projectile is buried within the F K x-ray peak and can not be separated. The K REC and RDEC do overlap somewhat, an obfuscation that will be addressed later. To separate REC and RDEC events from this raw spectrum a sorting algorithm must be applied.

Examples of singly (q-1) and doubly (q-2) charge-changed particle (TAC) spectra are shown in Fig. 17 a and 17 b, respectively. As stated previously, the counts in these spectra represent the time difference between detected x rays and charge-changed particles. Due to the inherent faster rise times for signals corresponding to higher-energy x rays, there will be a larger time difference between the charge-changed particles and higher-energy x rays

(because the TAC is started on the x rays) than for lower-energy x rays. This means that the high-channel events in these spectra are due to higher-energy x rays and, correspondingly, the low-channel events are due to lower-energy x rays. As seen in Fig. 16 b, there are far more x ray events on the low-energy side of the spectrum than the high-energy side due to the large number of characteristic projectile and target x rays. Also, there are slightly higher backgrounds below the peak than above in Figs. 17 a,b. The backgrounds are both fairly constant, with the slight exception of a shoulder at about channel 900 due to F K x rays. The REC photons will have a slightly higher energy than the F K x rays, and will therefore come at a higher channel in the TAC spectra due to the faster rise time, as previously discussed. As seen from Eqs. 2 and 4, RDEC photons will have a higher energy than REC photons and are expected to arrive on the high-time side of the peak in Fig. 17 b.

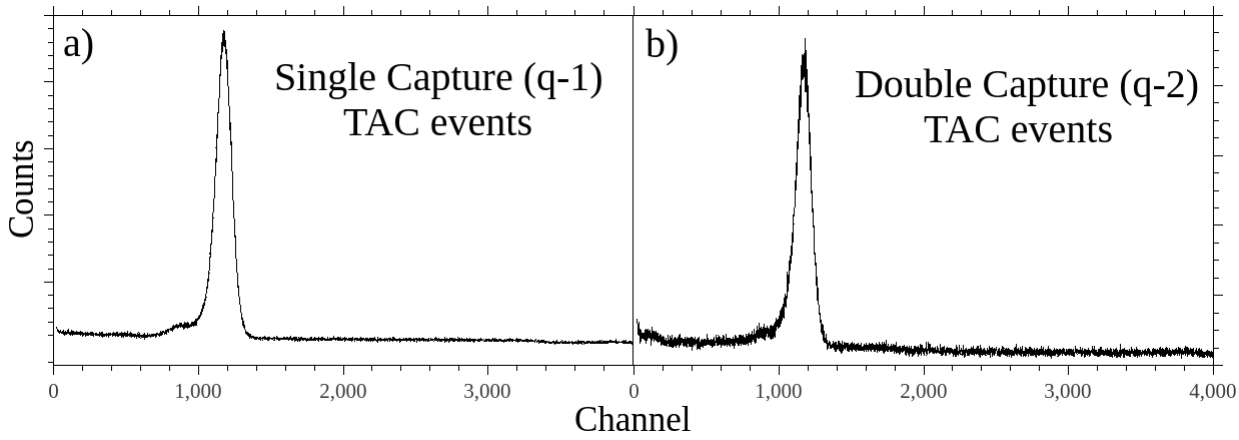

Figure 17: Example of a) single (q-1) and b) double (q-2) electron capture TAC spectra for 40 MeV F^{9+}+Ne (15 mTorr).

4.2 Coincidence Spectra

Coincidence in the context of this dissertation is defined as an emitted x ray associated with single or double electron capture or, conversely, single or double electron capture associated with an emitted x ray. The probability (cross section) of an RDEC event is expected to be low when compared with other types of capture events. As seen in Fig. 16 b, there are no discernible RDEC peaks. The x rays associated with single and double electron capture must therefore be separated from this raw x-ray spectrum for meaningful information to be extracted. As confirmation of a specific event like REC or RDEC, the single and double electron capture TAC events associated with photons from the energy region of that event should also be separated from the raw TAC spectra.

4.2.1 TAC-Gated X-Ray Spectra

Sorting windows must be chosen within one spectrum to yield the events from another spectrum associated with events from the initial spectrum. Several windows were chosen to ensure correct data analysis. A typical q-2 TAC spectrum with several sorting windows is shown in Fig. 18. After sorting with SpecTCL, x ray spectra will be generated with double or single electron capture. When applied to either the q-1 or q-2 TAC spectrum, the window associated with the entire peak (W_{pk}) gave spectra similar to Fig. 16 b, although with far fewer counts. The window from the low-time side of the peak (W_{low}) yielded a spectrum that included nearly all of the characteristic projectile and target x rays but with nearly zero counts beyond 2.5 keV. As discussed earlier, the REC and RDEC events are expected to come mainly from the high-time side of the TAC peak. A window was also set far beyond the TAC peak (W_{bkgd}) to evaluate the noise background and ensure the events identified as REC or RDEC are in fact due to those processes.

A window was initially set at the full height of the TAC peak extending to well beyond the peak (W_1). This did indeed decrease the number of characteristic projectile and target x rays while retaining the higher-energy x rays. The window size was sequentially decreased

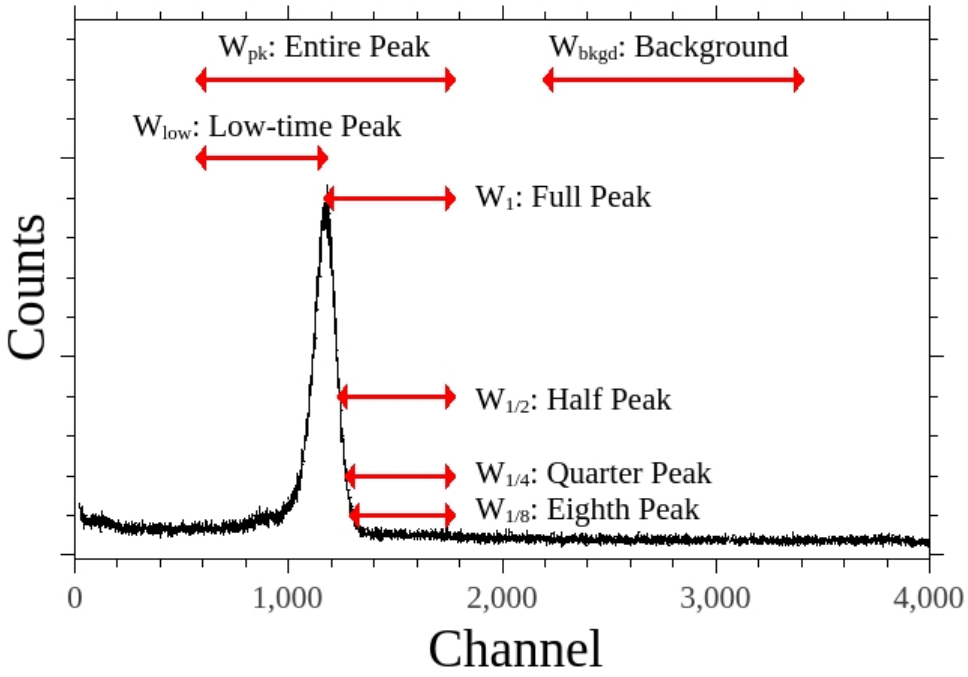

Figure 18: Sorting windows placed on TAC peak to give x rays associated with single or double electron capture.

until the number of x rays beyond 2 keV began to decrease significantly, making these spectra essentially background free. Additional windows were set at one half ($W_{1/2}$), one quarter ($W_{1/4}$), and one eighth ($W_{1/8}$) the peak height on the high-time side extending to the same point as the full height window. Ultimately the quarter height spectrum was chosen. Using window $W_{1/4}$, the x-ray spectrum associated with double electron capture after background subtraction are shown in Fig. 19. In that Figure, V refers to valence (quasi-free) electrons. Also shown in that figure are smooth curves representing the calculated Compton profiles of the transitions arbitrarily normalized to the data. The following scheme is used depending on the initial state of the transition: VV is indicated by the short dashed lines, VK by the long dashed lines, and KK by the solid lines. The q-2 TAC-gated x-ray spectra for F^{8+} shows sparse counts. The more convincing evidence of RDEC for the F^{8+} projectiles is revealed by the x ray-gated q-2 TAC spectra described in Section 4.2.2.

The REC and RDEC regions are well separated for N_2; however, this is not the case for Ne, for which the KK→KL RDEC transition lies directly under the K REC peak. For

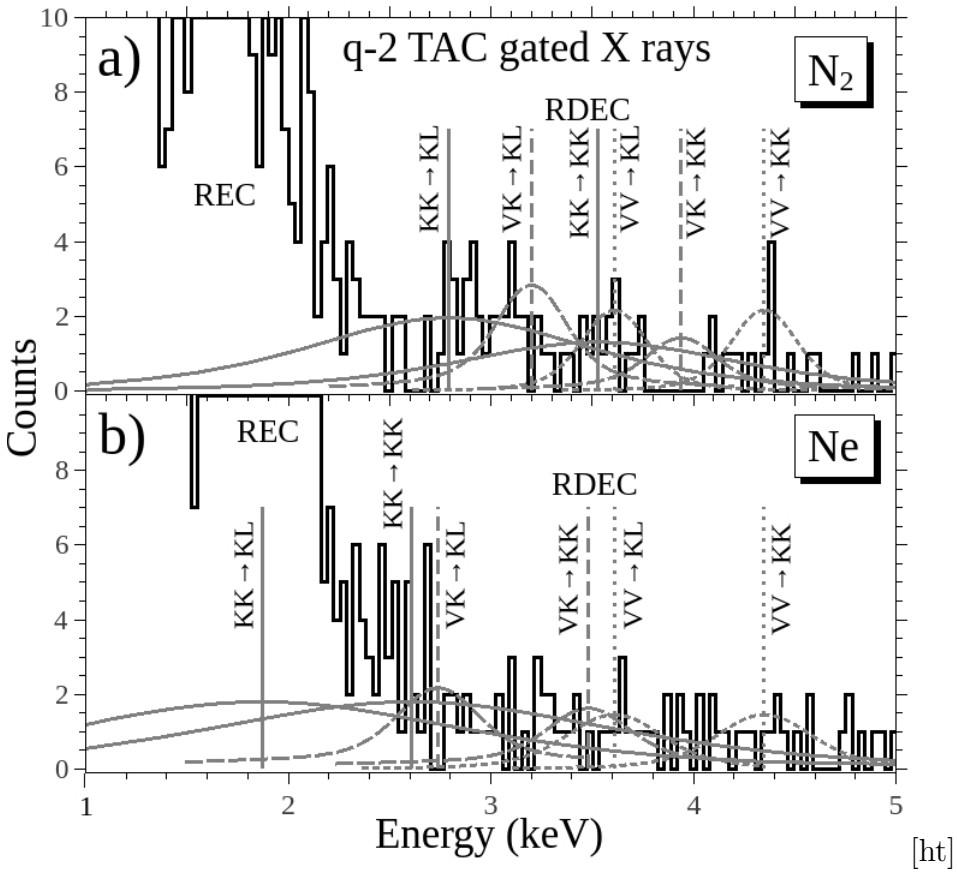

[ht]

Figure 19: X-ray spectra obtained from quarter-height ($W_{1/4}$) q-2 TAC peaks for F^{9+} a) N_2 (8 mTorr) and b) Ne (15 mTorr). V refers to valence (quasi-free) electrons. The smooth curves under the RDEC region show the calculated Compton profiles of the transitions arbitrarily normalized to the data. The following scheme is used depending on the initial state of the transition: VV is indicated by the short dashed lines, VK by the long dashed lines, and KK by the solid lines.

N_2, the KK→KK and VV→KL transitions are separated by less than the resolution of the x-ray detector and therefore cannot be evaluated separately. This is also the case for the KK→KK/VK→KL and VK→KK/VV→KL RDEC transitions in Ne. The number of RDEC counts from the spectra of panels (a) and (b) are ∼70 and ∼75 for N_2 and Ne, respectively.

4.2.2 X Ray-Gated Particle Spectra

In reverse fashion to the sorting algorithm described in Section 4.2.1, windows based on the energy of a given process can be placed on the obtained x-ray spectra to obtain single and double electron capture spectra associated with those photon energies. Sorting windows

were chose based on the position of the relevant REC and RDEC lines and their Compton profile widths. For REC, the lower limit of the window was placed just above the F K peak and the upper limit was placed at 150 eV above the K REC line. For RDEC, these windows were set at 300 eV below the KK→KL line for N_2 and 300 eV below the KK→KK line for Ne. The upper limit was positioned at 300 eV above the VV→KK line for both targets. These windows (green) are shown in Fig. 20 for clarity. The RDEC sorting window for Ne was truncated (red) when reaching the REC region so as to avoid double counting and over estimating the RDEC cross section. A window was also placed on the F K x-ray peak to confirm the expected x ray-gated TAC peak behavior, as discussed later.

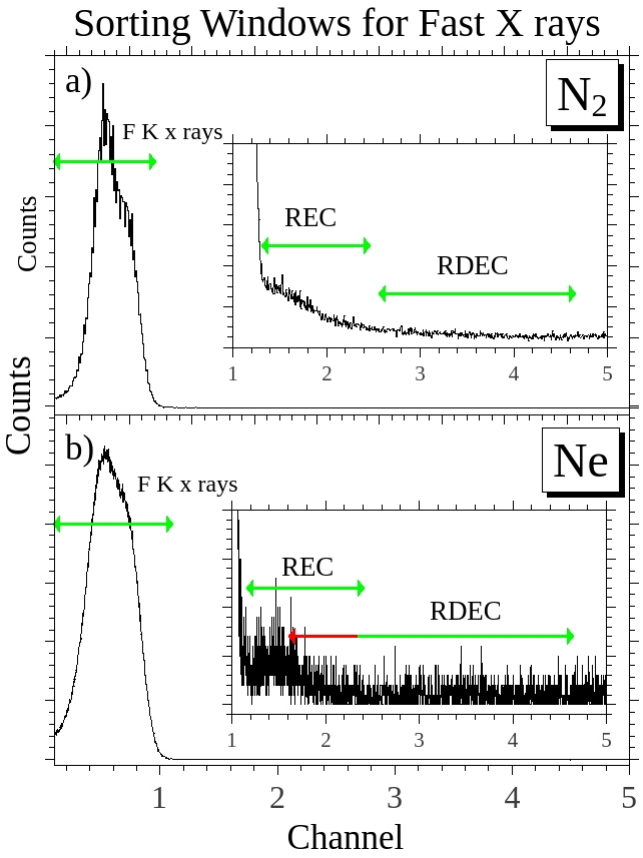

Figure 20: Sorting windows placed on FAST x-ray spectra for 40 MeV F^{9+} + a) N_2 (8 mTorr) and b) Ne (15 mTorr).

The resulting TAC spectra for F^{9+} (left column) and F^{8+} (right column) on N_2 and Ne are shown in Figs. 21 and 22, respectively. The spectra were integrated in the peak region and subsequently in equal-width background regions above and below the peak. The number of counts in the background regions after normalization were then subtracted from the number of peak counts to give the number of counts for the relevant process. These counts after background subtraction are given in the figures and compiled in Table 3. The probability of double electron capture for fully-stripped and one-electron fluorine at this beam energy is quite high. Thus, as seen, there are a significant number of REC events in the q-2 channel. The q-1 RDEC x ray-gated TAC channel showed a constant background with no discernible peak, as expected for low target densities and confirming single collision conditions.

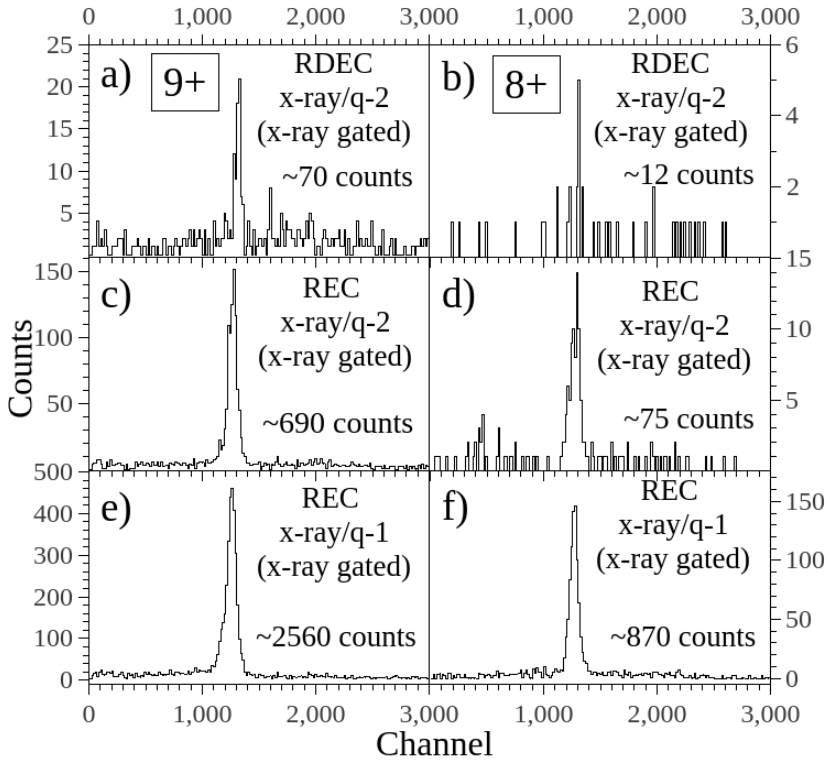

Figure 21: Spectra for 2.11 MeV /u F^{9+} (left column) and F^{8+} (right column) + N_2 (8 mTorr): (a),(b) q-2 TAC events from spectra similar to Fig. 17 b sorted on x rays from the RDEC energy range (Fig. 20 a); (c),(d) q-2 TAC events from spectra similar to Fig. 17 b and (e),(f) q-1 TAC events from spectra similar to Fig. 17 a sorted on x rays from the REC energy range (Fig. 20 a).

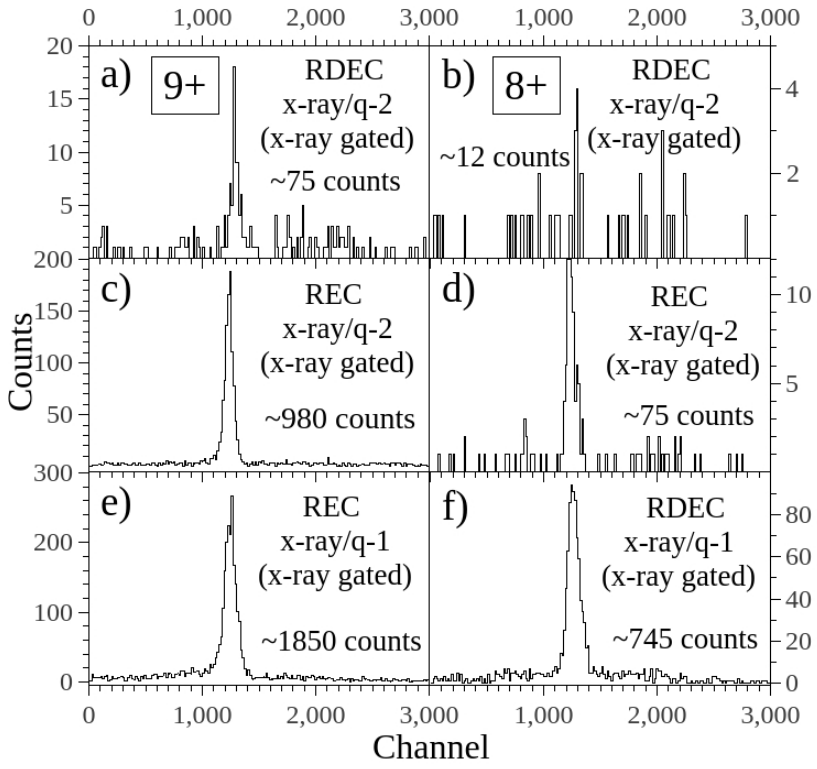

Figure 22: Spectra for 2.11 MeV /u F^{9+} (left column) and F^{8+} (right column) + Ne (15 mTorr): (a),(b) q-2 TAC events from Fig. 17 b sorted on x rays from the RDEC energy range (Fig. 20 b); (c),(d) q-2 TAC events from Fig. 17 b and (e),(f) q-1 TAC events from Fig. 17 a sorted on x rays from the REC energy range (Fig. 20 b).

The sorting algorithm was also applied to the F^{9+} x-ray spectra for N_2 and Ne around the specific RDEC transitions line at ±200 eV to the extent possible to give q-2 TAC peaks associated with those energy ranges. As mentioned previously, not all RDEC transition lines are resolvable. The sparse number of counts for the F^{8+} projectile did not allow this analysis. Those results are reported in Table 4.

Table 3: Counts obtained from x ray-gated TAC spectra for 40 MeV F^{9+} and F^{8+} + N_2 (Fig. 21) and Ne (Fig. 22).

		N_2 [59]		Ne	
		F^{9+}	F^{8+}	F^{9+}	F^{8+}
q-1	REC	2560	870	1850	745
q-2	REC	690	75	980	75
Total	REC	3250	945	2830	820
q-2	RDEC	70	12	75	12

Table 4: Counts obtained from x ray-gated TAC spectra for 40 MeV F^{9+} + N_2 (Fig. 21) and Ne (Fig. 22) for specific resolvable transitions.

RDEC	N_2 [59]	Ne	RDEC
KK→KL/VK→KL	37	-	under K REC peak
KK→KK/VV→KL	19	56	KK→KK/VK→KL
VK→KK	0	16	VK→KK/VV→KL
VV→KK	15	12	VV→KK

As a final check that the F K x rays come after (in time) the REC and RDEC photons in the TAC spectra, a window was placed on the F K x-ray peak as shown in Fig. 20. A comparison of the resulting x ray-gated q-2 TAC peaks is shown in Fig. 23 for a) F K photons, b) REC photons, and c) RDEC photons resulting from 40 MeV F^{9+} + Ne. As stated previously, the TACs START on the x rays and STOP on the charge-changed particles. High-energy x ray signals will have faster rise times in the electronics than those for low-energy x rays, therefore triggering the TACs earlier and creating a greater time delay between the signals (higher channel number). As can be seen, the peak centroid for doubly

charge-changed particles associated with F K photons comes at a significantly lower channel number than do the centroids of the peaks associated with the REC and RDEC photons. The REC peak centroid comes at a slightly lower channel number than the RDEC peak centroid. These differences in the peak centroids come from the good time resolution of the detector and are therefore due to differences in the rise times of the signals. The time (channel) difference between the centroids in Fig. 23 is consistent with the difference in the rise times for the associated x rays.

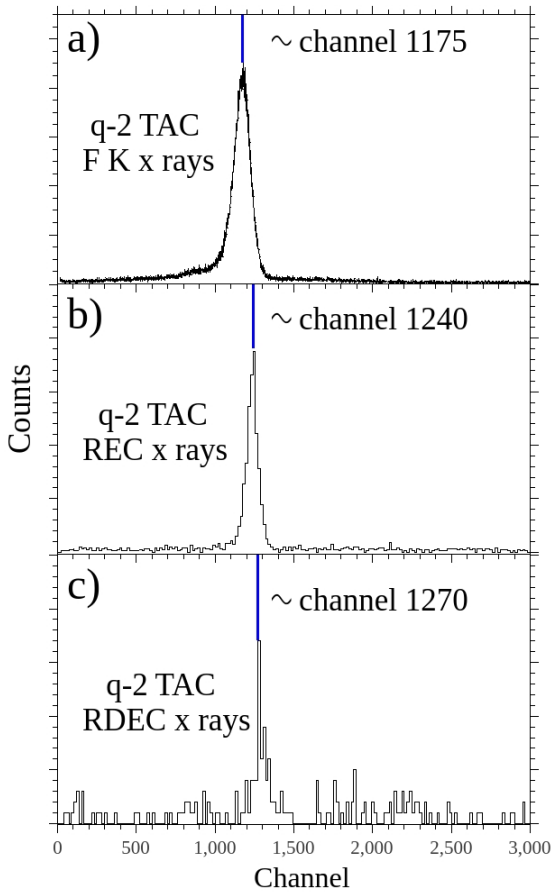

Figure 23: Spectra for 2.11 MeV /u F^{9+} + Ne (15 mTorr) double charge-exchange (q-2) associated with: (a) F K x rays, (b) REC x rays, and (c) RDEC x rays.

4.3 RDEC and REC Cross Section Calculations

For any collision event where x-ray emission or charge exchange takes place, the beam fraction (F) for that process is given as the ratio of the number of events (x rays or charge-changed particles) to the total incident beam. This fraction is a function of the target density (gas pressure P), and under single-collision conditions is a linear function: $F = \kappa P$, where κ is proportional to the cross section. The fraction F is also necessarily proportional to the time of interaction, i.e., the length of the cell. When determining the cross section for an emitted x-ray, the detector efficiency ϵ and solid angle $\Delta\Omega$ must necessarily be included. Here, $\Delta\Omega$ is the detector area (60 mm^2) divided by the distance to the detector crystal (17 mm^2) squared ($\approx \frac{A}{r^2}$).

The fraction F was determined by dividing the number of relevant events (the process described later in this section) by the total number of incident particles obtained from the beam current and particle detectors. The differential cross section for an event where an x ray is emitted following charge exchange is given as the following:

$$\frac{d\sigma}{d\Omega_\theta} = \frac{\Delta F}{\Delta P}\frac{1}{N_o L}\frac{1}{\epsilon\Delta\Omega} \tag{5}$$

where ΔF is the change in the beam fraction, ΔP is the change in pressure related to ΔF, $N_o = 3.30 * 10^{13}\ [mT * cm^3]^{-1}$ is the target density factor, and L is the length of the cell (3.65 cm).

4.3.1 Pile-up Effect

For the collision system of interest here, it has been shown that the energy of an RDEC photon is approximately double that of an REC photon. The possibility does exist that the x-ray detector could absorb simultaneously two REC photons that register as a single photon of double energy, which would therefore be indistinguishable from a single RDEC photon, known as pile-up. These two REC photons would most likely come from a single ion

undergoing REC twice from a single collision event (DREC). The cross section for double REC has been shown to scale as follows [60]:

$$\sigma_{\mathrm{DREC}} \propto (\frac{\sigma_{\mathrm{REC}}}{\mathrm{a_0}})^2$$

where $\mathrm{a_0}$ is the Bohr radius and $\sigma_{\mathrm{REC}} \ll \mathrm{a_0}$. This makes the probability of double REC observation at least two orders of magnitude smaller than that for RDEC and therefore it can be neglected. Double REC from multiple collisions are possible; however, the explicit tuning of the target density to remove multiple-collision conditions makes this sequence of events negligible. It is also possible that two ions will separately undergo REC. This situation is also highly unlikely, as the beam density is intentionally kept low.

4.4 Results

Photon emission due to REC into the K shell of bare ions has been shown to be linearly polarized [61, 62], introducing an angular dependence of $\sin^2\theta$ between the differential and total cross sections. The present work assumes that the differential cross section measured for RDEC behaves in the same manner. Therefore, integrating over the polar coordinates introduces a factor of $8\pi/3$ to the total cross section. It is noted, however, that electron correlation in RDEC may affect the polarization of the emitted photon, invalidating this assumption.

Systematic errors in the electronics include the uncertainty in the beam measurement from the Keithley electrometer, the pressure accuracy of the capacitance manometer, the physical dimensions mentioned above, and the counting of the charge-changed particles. The efficiency of the x-ray detector has also been considered as previously mentioned. All of these systematic errors are much less than the relative errors for the cross sections.

Given the number of counts for the relevant process in Table 4 the differential and total cross sections can be calculated from Eq. 5. The differential and total cross sections for

40 MeV F^{9+} and F^{8+} projectiles incident on target N_2 and Ne gases are given in Table 5. The RDEC cross sections for Ne may be underestimated by up to a factor of 2 because the KK $\rightarrow$ KL transition under the REC peak could not be seen, and that transition is expected to have a significant contribution to the RDEC cross section [13]. The differential and total RDEC cross sections for the specific resolvable transitions from Table 4 are given in Table 6. The number of counts for these transitions were determined by setting windows on the x-ray spectra around the transition centroids whose widths were based on the width of the Compton profiles and sorting those data to give doubly charge-changed particle spectra, as discussed previously.

It might be expected that the presence of one K-shell vacancy (F^{8+} projectiles) instead of two (F^{9+} projectiles) in the incident ion would decrease the RDEC cross section by a factor of two or four, as both electrons cannot be captured to the KK shells. However, the RDEC cross sections were found to be lower by a factor of $\sim$6. At present, we do not know the explanation for this effect, but a possible explanation is that the initial states in the target play a role in the probability of being captured to certain final states in the projectile. Obviously, this point needs further investigation, probably both experimentally and theoretically.

Table 5: REC and RDEC differential ($\frac{d\sigma}{d\Omega}$) at 90° (barns/sr) and total (σ) (barns) cross sections for 2.11 MeV/u $F^{9+,8+} + N_2$ and Ne. The REC cross sections are likely underestimated because all of the REC events could not be extracted from the F K x rays. The numbers in parentheses indicate the uncertainties in the cross sections listed.

		N_2 [59]		Ne	
		$\frac{d\sigma}{d\Omega}$	σ	$\frac{d\sigma}{d\Omega}$	σ
REC	F^{9+}	14.0(8.8)	118(74)	10.3(6.5)	86.2(54.2)
	F^{8+}	4.0(2.6)	33.5(21.4)	3.3(2.1)	27.6(18.0)
RDEC	F^{9+}	0.30(0.17)	2.5(1.4)	0.25(0.14)	2.1(1.2)
	F^{8+}	0.05(0.03)	0.42(0.25)	0.04(0.02)	0.33(0.20)

Table 6: RDEC differential ($\frac{d\sigma}{d\Omega}$) at 90° (mb/sr) and total (σ) (barns) cross sections for specific resolvable RDEC transitions for 2.11 MeV/u $F^{9+} + N_2$ and Ne. The numbers in parentheses indicate the uncertainties in the cross sections listed.

	N_2 [59]	
RDEC	$\frac{d\sigma}{d\Omega}$	σ
KK→KL/VK→KL	159(91)	1.3(0.74)
KK→KK/VV→KL	81.7(46.9)	0.68(0.39)
VK→KK	10.7(10.7)	0.09(0.09)
VV→KK	64.5(37.0)	0.54(0.31)
	Ne	
under K REC peak	-	-
KK→KK/VK→KL	182(104)	1.52(0.86)
VK→KK/VV→KL	51.8(29.2)	0.43(0.25)
VV→KK	38.9(22.3)	0.33(0.19)

5 Discussion

The cross section results for RDEC to the projectile KL and KK shells described in Section 2.5.1 and 2.5.2 are summarized in Table 7 along with the results of this dissertation. Many of the ratios from the various theories are calculated using the Sommerfeld parameter [13] given as:

$$\kappa = \frac{p_{ep}}{p_{et}} = \frac{v_{ep}}{v_{et}} = \frac{Z_p e^2}{\hbar v_p}$$

where p_{ep} (v_{ep}) is the average momentum (velocity) of the target electron after capture to the projectile K shell, p_{et} (v_{et}) is the momentum (velocity) of the target electron that will be captured in the rest frame of the projectile, v_p is the velocity of the projectile, and Z_p is the atomic number of the projectile.

As can be seen, all of the theories underestimate the presented experimental results, with some being as many as four [63] orders of magnitude smaller. This is likely due to the assumptions made in the theories, especially the ones only considering capture from the target K shell. Also, nearly all of the theoretical considerations were performed prior to successful experimental confirmation of the process [14]. The prior successful experimental results, along with the results presented herein, will hopefully lead to a reevaluation of the theoretical assumptions and models.

The σ^{KL}_{RDEC} results for F^{9+} + C are slightly higher than those for O^{8+} + C. This is likely due to the slightly lower projectile energy and the higher projectile Z_p. With the same fluorine projectile and a slightly lower energy, the results for the N_2 and Ne targets are both lower. However, it must be remembered that the KK→KL transition is not included in σ^{KL}_{RDEC} for Ne due to the fact that it is under the REC peak for this target (see Fig. 20). This suggests that σ^{KL}_{RDEC} decreases with target Z_t because the identical projectile (with just slightly lower energy) incident on heavier (higher Z_t) targets results in lower σ^{KL}_{RDEC}.

The first experimental results for Ar^{18+} [7] and U^{92+} [8] projectiles reported upper limits on σ^{KK}_{RDEC} that are also two or three orders of magnitude lower than the results for F^{9+},

although for different energy projectile-target systems. The σ^{KK}_{RDEC} results for F^{9+} + C are again slightly larger than those for O^{8+} + C, presumably also due to the lower projectile energy and the higher projectile Z_p. The results for F^{9+} + N_2 and Ne are both lower than those for the same projectile incident on the carbon target. This suggests that σ^{KK}_{RDEC} decreases with target Z_t in the same way as σ^{KL}_{RDEC}.

For both O^{8+} and F^{9+} + C, σ^{KL}_{RDEC} and σ^{KK}_{RDEC} are equal within their uncertainties, with the former being reported as slightly smaller. For F^{9+} + N_2 the situation is reversed, with the latter being reported as slightly smaller. When one again considers the uncertainties involved, this may not necessarily be the case. Again, the KK→KL transition is not included in σ^{KL}_{RDEC} for Ne. Here, σ^{KL}_{RDEC} and σ^{KK}_{RDEC} are found to be approximately equal in magnitude for low-Z ($\leq$10), low-energy ($\leq$2.5 MeV/u) projectiles on low-Z targets.

The $\sigma^{KL}_{RDEC}/\sigma^{KK}_{RDEC}$ ratios are shown in the fourth major column in the table. As the paper by Nefiodov *et al* [13] is the only theoretical work to consider the KL-RDEC transition, it is the only theory listed in this column. For O^{8+} and F^{9+} + C the theoretical results are nearly identical to the experimental results. However, this is not the case for F^{9+} + N_2 where the experimental result is about a factor of two larger than the theoretical result. This may be due to the heavier target (higher Z_t). The theoretical result for F^{9+} + Ne appears to overestimate the experimental result somewhat. However, one must recall that the KK→KL transition has not been included. That transition is expected to be significant based on the results for the N_2 target (see Table 7) and the true $\sigma^{KL}_{RDEC}/\sigma^{KK}_{RDEC}$ ratio for Ne is likely larger, possibly by a factor of two.

The $\sigma^{KL}_{RDEC}/\sigma^{KK}_{RDEC}$ ratio for O^{8+} + C is slightly smaller ($\sim$20%) than for F^{9+} + C for both the theoretical and experimental results. The F^{9+} + N_2 ratio is about a factor of two larger than for the carbon target. If both cross sections behave in the manner discussed previously with target Z_t, this behavior is likely due to the heavier target and possibly the slightly lower projectile energy. The result for F^{9+} + Ne is the smallest, being about a factor of three smaller than for the N_2 target.

Table 7: Experimental and theoretical total cross sections for capture to the projectile KL shells (σ^{KL}_{RDEC}) or KK shells (σ^{KK}_{RDEC}) in barn/atom. Parentheses behind the numbers indicate the uncertainties and brackets indicate multiplication by powers of 10.

Projectile	Energy (MeV/u)	κ	Target	σ^{KL}_{RDEC} Che [47]	σ^{KL}_{RDEC} Nef [13]	σ^{KL}_{RDEC} Exp	σ^{KK}_{RDEC} Mist [48]	σ^{KK}_{RDEC} Mik [63]	σ^{KK}_{RDEC} Yak [11]	σ^{KK}_{RDEC} Exp	$\sigma^{KL}_{RDEC}/\sigma^{KK}_{RDEC}$ Nef [13]	$\sigma^{KL}_{RDEC}/\sigma^{KK}_{RDEC}$ Exp
Ar^{18+} [7]	11.4	0.84	C		2.2[-3]		0.12^{A} $4.3[-3]^{K}$	$3.5[-3]^{2K}$ $2.9[-6]^{2V}$	1.9[-3]	≤5.2[-3]	0.63	
U^{92+} [8]	297	0.84	Ar		1.7[-5]		$1.7[-3]^{A}$ $3.1[-6]^{K}$	$2.7[-5]^{2K}$ $8.4[-10]^{2V}$	5.0	≤1.0[-2]	0.63	
Cr^{24+} [9]	30	0.69	He								0.57	
Cr^{24+} [9]	30	0.69	N_2								0.57	
O^{8+} [14]	2.38	0.82	C	0.05^{A} $2.0[-3]^{K}$	0.10	2.3(1.3)	0.55^{A} 0.02^{K}	0.14^{2K} $1.2[-4]^{2V}$	0.14	3.2(1.9)	0.70	0.72(0.07)
F^{9+} [15]	2.21	0.96	C		0.24	4.5(1.8)	0.94^{A} 0.03^{K}	0.27^{2K} $2.2[-4]^{2V}$	0.18	4.6(2.8)	0.90	0.96(0.70)
F^{9+} [59]	2.11	0.99	N_2		0.38	1.7(1.0)		0.49^{2K} $4.0[-4]^{2V}$	0.18	0.86(44)	0.91	2.0(1.6)
F^{8+} [59]	2.11	0.99	N_2			0.42(0.25)	-	-	-	-	-	-
F^{9+}	2.11	0.99	Ne		1.11	0.98(0.56)*†		1.4^{2K} $1.2[-3]^{2V}$	0.18	1.3(0.7)*	0.91	0.68(0.54)*†
F^{8+}	2.11	0.99	Ne			0.33(0.20)	-	-	-	-	-	-

[A]Considers all the atoms in the target.
[K]Considers just K-shell electrons in the target.
[2K]Capture of two K-shell electrons.
[2V]Capture of two valence electrons.
*Estimated by dividing unresolvable transition counts in Table 6 by two.
†Does not include KK → KL transition under the K REC peak.

Shown in Fig. 24 are the present experimental results for N_2 and Ne gas targets, as well as the previous experimental results for fully-stripped projectiles on thin-foil C targets and the relevant theories that most closely reproduce the experimental results. It is seen that the results for RDEC with F^{9+} on N_2 and Ne are factors of ∼2 (for O^{8+}) and 4 (for F^{9+}) times smaller than those for the carbon target, although the value for F^{9+} on Ne may be somewhat larger. The theories underestimate the experimental data by about an order of magnitude and up to three orders of magnitude. This is likely due to the assumptions made in the theories to simplify the calculations. The work of Ref. [48] employs the line-profile approach for the two models shown, both with homogeneous target electron densities: model A considers all the electrons in the target equally and model K considers only the target K-shell electrons. There are presently no calculations for F^{9+} on gas targets but it is expected that they would not differ greatly from those for carbon.

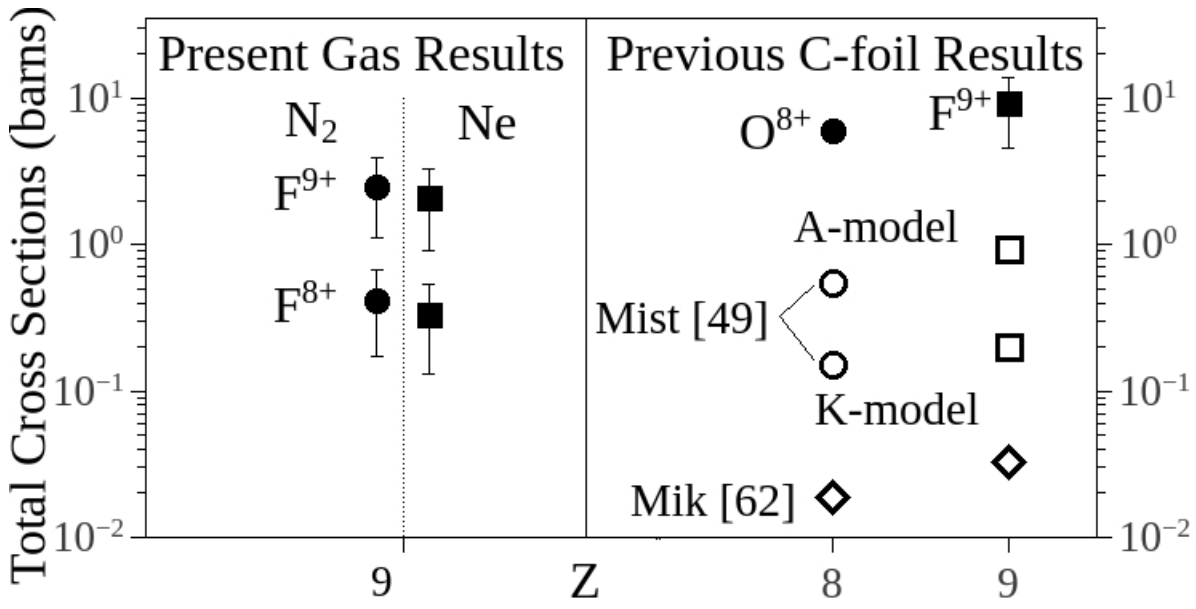

Figure 24: Present results for F^{9+} and F^{8+} projectiles on N_2 and Ne targets (left panel); previous results for fully-stripped O^{8+} and F^{9+} projectiles on C targets (right panel). The A- and K-models are from Ref. [48].

Finally, measurements were performed for 40 MeV F^{9+} + He. Investigation of RDEC for the capture of the two K-shell electrons in He targets would be highly desirable, as only two transitions are possible, namely KK→KK and KK→KL (only the KK→KL would be possible for F^{8+} projectiles). This would give valuable information on the nature of RDEC as it pertains to the initial state(s) of the captured electrons. The measurements were ultimately terminated for practical reasons because of the very low counting rate, for which just three RDEC events were observed in two weeks of round-the-clock beamtime.

6 Conclusion

This dissertation has presented conclusive evidence for the existence of radiative double electron capture (RDEC) for fully-stripped and one-electron projectiles colliding with N_2 and Ne gas targets. RDEC can be considered the time-inverse of double photoionization, a process for which observance in the laboratory can be quite challenging to realize, depending on the energy of the photon and the target species or ionization state. As such, this work represents a step forward in the understanding of both processes.

Measurements were performed for 2.11 MeV/u F^{9+} and F^{8+} incident on N_2 and Ne using the tandem Van de Graaff accelerator facility at Western Michigan University (WMU). The results were compared for the two charge states and with the previous experimental results for various energy projectile-target systems and, most appropriately, with the results for fully-stripped oxygen [14] and fluorine [15] projectiles incident on thin-foil carbon targets that were also performed at WMU. These previous carbon results exhibited multiple-collision effects for both projectiles, which somewhat clouded the results, an obfuscation not present with gas targets whose pressures can be set to single-collision conditions. Contaminants sometimes present with carbon foils [15] are also essentially eliminated for gas targets. All experimental results were compared with various theoretical predictions to the extent possible. No theory yet exists specifically for the collision systems done here.

The total RDEC cross sections determined in this work for F^{9+} incident on N_2 and Ne were 2.5 $\pm$ 1.4 b/atom and 2.1 $\pm$ 1.2 b/atom, respectively. It is noted, however, that the KK$\rightarrow$KL transition for the Ne target could not be included in the cross section, as it lies under the K-shell REC peak. Comparison of bare fluorine on N_2 and Ne gas targets with previous experimental results for O^{8+} and F^{9+} on carbon showed smaller cross sections by factors of about 2-4 for the present results.

RDEC to the projectile KL and KK shells were separated to the extent possible. The results for Ne were again clouded by the fact that the KK$\rightarrow$KL transition was unresolvable from REC transitions. RDEC to the KL and KK shells were found to be comparable for the

carbon targets. For the N_2 target, however, the cross section for RDEC to the KL shells was a factor of ∼2-3 larger than to the KK shells. The Ne target showed the two cross sections to be comparable, but the results likely would have been in agreement with those for N_2 if the KK→KL transition had been discernible for the Ne target. The gas target results therefore support the calculations of Nefiodov *et al* [13] that RDEC to the excited 2^1S state of heliumlike ions is more likely than capture to the ground 1^1S state.

The total cross sections for RDEC to one-electron fluorine (F^{8+}) ions incident on N_2 and Ne were also reported, with the results being 0.42 ± 0.25 b/atom and 0.33 ± 0.20 b/atom, respectively. The factor of ∼6 difference between the F^{9+} and F^{8+} results, as opposed to a factor of ∼2 or 4 that one might expect, cannot be fully explained but is presumably due to the presence of one K-shell vacancy instead of two vacancies. Observation of RDEC for one-electron projectiles supports the assertion that RDEC to the KL shells plays a significant role in the process.

In summary, RDEC has been successfully observed for bare and one-electron fluorine ions striking gas N_2 and Ne targets. The measurements were done under single-collision conditions to prevent complications from multiple collision events. High purity target gases were used to minimize the effects of contaminants. Cross sections for both projectiles were determined and compared with theoretical calculations to the extent possible, as well as with each other. Individual RDEC transitions were also determined to the extent possible. Not only has the RDEC process been confirmed experimentally, its observation with gas targets has been shown and RDEC transitions to the projectile KL shells appears to be more (or as) significant as capture to the projectile KK shells.

In the future, an RDEC polarization study would be highly useful to either confirm or disprove the REC-like emission behavior assumed in this work. A study with a He target would also be of great use in that only target KK transitions are possible and the $\sigma^{\mathrm{KL}}_{\mathrm{RDEC}}/\sigma^{\mathrm{KK}}_{\mathrm{RDEC}}$ ratio could be determined from those data; such a study requires significant beam time and resource investments as noted previously. The group of Dr. Tanis at WMU

is currently confirming and extending the previous solid-target RDEC results by executing 35 MeV $O^{8+,7+}$ and 40 MeV $F^{9+,8+}$ projectiles incident on carbon. The group also plans to study RDEC for swift projectiles incident on graphene, a two-dimensional carbon target.

References

[1] L. D. Landau and E. M. Lifszyc, *Mechanika kwantowa and Teorianierelatywistyczna*. PWN Warszawa, 1979.

[2] H. F. Beyer and V. P. Shevelko, *Introduction to the Physics of Highly Charged Ions*. CRC Press, 1st ed., 2002.

[3] L. Gildart and A. W. Ewald, "Electron mobility and luminescence efficiency in cadmium sulfide," *Phys. Rev.*, vol. 83, pp. 359–363, Jul 1951.

[4] H. W. Schnopper, H. D. Betz, J. P. Delvaille, K. Kalata, A. R. Sohval, K. W. Jones, and H. E. Wegner, "Evidence for radiative electron capture by fast, highly stripped heavy ions," *Phys. Rev. Lett.*, vol. 29, pp. 898–901, Oct 1972.

[5] T. Stöhlker *et al.*, "Radiative electron capture studied in relativistic heavy-ion–atom collisions," *Phys. Rev. A*, vol. 51, pp. 2098–2111, Mar 1995.

[6] J. Miraglia and M. S. Gravielle, *International Conference on Photonic, Electronic and Atomic Collisions XV: Book of Abstracts*. 1987. Brighton, U.K.

[7] A. Warczak *et al.*, "Radiative double electron capture in heavy-ion atom collisions," *Nuclear Instruments and Methods in Physics Research B*, vol. 98, pp. 303–306, 1995.

[8] G. Bednarz *et al.*, "Double electron capture in relativistic U^{92+} collisions at the ESR gas-jet target," *Nuclear Instruments and Methods in Physics Research B*, vol. 205, pp. 573–576, 2003.

[9] N. Winters *et al.*, "A study of radiative double electron capture in bare chromium ions at the ESR," *Physica Scripta*, vol. T156, no. 014048, 2013.

[10] V. L. Yakhontov and M. Y. Amusia, "Radiative double electron capture in fast heavy ion-atom collisions," *Physics Letters A*, vol. 221, pp. 328–334, 1996.

[11] V. L. Yakhontov and M. Y. Amusia, "Radiative double-electron capture in collisions of fast heavy ions with solid carbon targets," *Phys. Rev. A*, vol. 55, pp. 1952–1961, Mar 1997.

[12] A. I. Mikhailov, I. A. Mikhailov, A. N. Moskalev, A. V. Nefiodov, G. Plunien, and G. Soff, "Nonrelativistic double photoeffect on K-shell electrons," *Phys. Rev. A*, vol. 69, p. 032703, Mar 2004.

[13] A. V. Nefiodov, A. I. Mikhailov, and G. Plunien, "Correlated radiative capture of two electrons with formation of heliumlike ion in the 1s2s ^1S state," *Physics Letters A*, vol. 346, pp. 158–162, 2005.

[14] A. Simon, A. Warczak, T. ElKafrawy, and J. A. Tanis, "Radiative double electron capture in collisions of O^{8+} ions with carbon," *Phys. Rev. Lett.*, vol. 104, p. 123001, Mar 2010.

[15] T. Elkafrawy, A. Simon, J. A. Tanis, and A. Warczak, "Single-photon emission associated with double electron capture in F^{9+}+C collisions," *Phys. Rev. A*, vol. 94, p. 042705, Oct 2016.

[16] H. Hertz, "Ueber den einfluss des ultravioletten lichtes auf die electrische entladung," *Annalen der Physik*, vol. 267, no. 8, pp. 983–1000, 1887.

[17] A. Einstein, "Über einen die erzeugung und verwandlung des lichtes betreffenden heuristischen gesichtspunkt," *Annalen der Physik*, vol. 17, no. 6, pp. 132–148, 1905.

[18] H. W. Schnopper, J. P. Delvaille, K. Kalata, A. R. Sohval, M. Abdulwahab, K. W. Jones, and H. E. Wegner, "X-ray measurements of bremsstrahlung and electron capture by fast positive ions," *Physics Letters A*, vol. 47, pp. 61–62, Feb 1974.

[19] D. J. Griffiths, *Introduction to Electrodynamics*. Prentice Hall, 3rd ed., 1999.

[20] K. Ishii and S. Morita, "Scaling law for a continuum of x-rays produced by light-ion-atom collisions," *Nuclear Instruments and Methods in Physics Research B*, vol. 22, pp. 68–71, Mar 1987.

[21] J. A. Tanis, E. M. Bernstein, W. G. Graham, M. Clark, S. M. Shafroth, B. M. Johnson, K. W. Jones, and M. Meron, "Resonant behavior in the projectile x-ray yield associated with electron capture in S + Ar collisions," *Phys. Rev. Lett.*, vol. 49, pp. 1325–1328, Nov 1982.

[22] D. Brandt, "Resonant transfer and excitation in ion-atom collisions," *Phys. Rev. A*, vol. 27, pp. 1314–1318, Mar 1983.

[23] J. A. Tanis, E. M. Bernstein, W. G. Graham, M. P. Stockli, M. Clark, R. H. McFarland, T. J. Morgan, K. H. Berkner, A. S. Schlachter, and J. W. Stearns, "Resonant electron transfer and excitation in two-, three-, and four- electron ${}_{20}\mathrm{Ca}^{q+}$ and ${}_{23}\mathrm{V}^{q+}$ ions colliding with helium," *Phys. Rev. Lett.*, vol. 53, pp. 2551–2554, Dec 1984.

[24] H. S. W. Massey and D. R. Bates, "The properties of neutral and ionized atomic oxygen and their influence on the upper atmosphere," *Reports on Progress in Physics*, vol. 9, pp. 62–74, jan 1942.

[25] A. Burgess, "Delectronic Recombination and the Temperature of the Solar Corona.," *Astrophysical Journal*, vol. 139, pp. 776–780, Feb. 1964.

[26] J. Eichler and T. Stohlker, "Radiative electron capture in relativistic ion-atom collisions and the photoelectric effect in hydrogen-like high- z systems," *Physics Reports*, vol. 439, no. 1–2, pp. 1–99, 2007.

[27] P. Kienle, M. Kleber, B. Povh, R. M. Diamond, F. S. Stephens, E. Grosse, M. R. Maier, and D. Proetel, "Radiative capture and bremsstrahlung of bound electrons induced by heavy ions," *Phys. Rev. Lett.*, vol. 31, pp. 1099–1102, Oct 1973.

[28] E. Spindler, H. D. Betz, and F. Bell, "Influence of retardation on the angular distribution of radiative electron capture," *Phys. Rev. Lett.*, vol. 42, pp. 832–835, Mar 1979.

[29] T. Stöhlker, H. Geissel, H. Irnich, T. Kandler, C. Kozhuharov, P. H. Mokler, G. Münzenberg, F. Nickel, C. Scheidenberger, T. Suzuki, M. Kucharski, A. Warczak, P. Rymuza, Z. Stachura, A. Kriessbach, D. Dauvergne, B. Dunford, J. Eichler, A. Ichihara, and T. Shirai, "l-subshell resolved photon angular distribution of radiative electron capture into He-like uranium," *Phys. Rev. Lett.*, vol. 73, pp. 3520–3523, Dec 1994.

[30] T. Stöhlker, F. Bosch, A. Gallus, C. Kozhuharov, G. Menzel, P. H. Mokler, H. T. Prinz, J. Eichler, A. Ichihara, T. Shirai, R. W. Dunford, T. Ludziejewski, P. Rymuza, Z. Stachura, P. Swiat, and A. Warczak, "Strong alignment observed for the time-reversed photoionization process studied in relativistic collisions with bare uranium ions," *Phys. Rev. Lett.*, vol. 79, pp. 3270–3273, Oct 1997.

[31] T. Stöhlker, T. Ludziejewski, H. Reich, F. Bosch, R. W. Dunford, J. Eichler, B. Franzke, C. Kozhuharov, G. Menzel, P. H. Mokler, F. Nolden, P. Rymuza, Z. Stachura, M. Steck, P. Swiat, A. Warczak, and T. Winkler, "Charge-exchange cross sections and beam lifetimes for stored and decelerated bare uranium ions," *Phys. Rev. A*, vol. 58, pp. 2043–2050, Sep 1998.

[32] J. A. Tanis, S. M. Shafroth, J. E. Willis, and J. R. Mowat, "Radiative electron capture by Cl ions incident on C and Cu foils," *Phys. Rev. A*, vol. 23, pp. 366–370, Jan 1981.

[33] J. Eichler, A. Ichihara, and T. Shirai, "Photon angular distributions from radiative electron capture in relativistic atomic collisions," *Phys. Rev. A*, vol. 51, pp. 3027–3035, Apr 1995.

[34] K.-i. Hino and T. Watanabe, "Angular-distribution and linear-polarization correlation of photons induced by the relativistic radiative electron-capture process," *Phys. Rev. A*, vol. 36, pp. 5862–5865, Dec 1987.

[35] A. Ichihara, T. Shirai, and J. Eichler, "Radiative electron capture in relativistic atomic collisions," *Phys. Rev. A*, vol. 49, pp. 1875–1884, Mar 1994.

[36] A. Ichihara, T. Shirai, and J. Eichler, "Radiative electron capture and the photoelectric effect at high energies," *Phys. Rev. A*, vol. 54, pp. 4954–4959, Dec 1996.

[37] A. R. Sohval, J. P. Delvaille, K. Kalata, and H. W. Schnopper, "Cross section ratio for radiative electron capture to inner and outer atomic shells," *Journal of Physics B: Atomic, Molecular and Optical Physics*, vol. 9, no. 4, pp. L47–L51, 1976.

[38] F. Biggs, L. B. Mendelsohn, and J. B. Mann, "Hartree-Fock compton profiles for the elements," *Atomic Data and Nuclear Data Tables*, vol. 16, no. 3, pp. 201–309, 1975.

[39] R. Shakeshaft and L. Spruch, "Mechanisms for charge transfer (or for the capture of any light particle) at asymptotically high impact velocities," *Rev. Mod. Phys.*, vol. 51, pp. 369–405, Apr 1979.

[40] H. Tawara, T. Azuma, T. Ito, K. Komaki, Y. Yamazaki, T. Matsuo, T. Tonuma, K. Shima, A. Kitagawa, and E. Takada, "X rays from radiative electron capture into continuum states in relativistic heavy-ion collisions," *Phys. Rev. A*, vol. 55, pp. 808–811, Jan 1997.

[41] G. Bednarz, A. Warczak, P. Swiat, T. Stohlker, H. Beyer, F. Bosch, R. W. Dunford, S. Hagmann, E. P. Kanter, C. Kozhuharov, A. Kramer, D. Liesen, T. Ludziejewski, X. Ma, P. H. Mokler, and Z. Stachura, "Double electron capture in relativistic U^{92+} collisions observed at the ESR gas-jet target," *Physica Scripta*, vol. T92, pp. 429–431, 2001.

[42] A. Simon, A. Warczak, and J. A. Tanis, "Observation of radiative double electron capture during O^{8+} collisions: Comparison with monte carlo simulation," *Physica Scripta*, vol. T144, no. 014024, 2011.

[43] T. Elkafrawy, A. Warczak, A. Simon, and J. A. Tanis, "Single-photon emission correlated to double-electron capture by bare ions: Background processes," *Physica Scripta*, vol. T156, no. 014047, 2013.

[44] T. Elkafrawy, A. Warczak, A. Simon, and J. A. Tanis, "Evidence for radiative double electron capture (RDEC) in F^{9+} on carbon collisions," *AIP Conference Proceedings*, vol. 64, pp. 64–67, 2013.

[45] A. B. Voitkov, B. Najjari, N. Toshima, and J. Ullrich, "Two-electron capture with emission of one photon in fast collisions between a highly charged ion and a light atom," *Journal of Physics B: Atomic, Molecular and Optical Physics*, vol. 39, pp. 3403–3417, 2006.

[46] E. G. Drukarev, A. I. Mikhailov, I. A. Mikhailov, and W. Scheid, "High-energy two-electron capture with emission of a single photon," *Phys. Rev. A*, vol. 76, p. 062701, Dec 2007.

[47] E. A. Chernovskaya, O. Y. Andreev, and L. N. Labzowsky, "Radiative double-electron capture by bare nucleus with emission of one photon," *Phys. Rev. A*, vol. 84, p. 062515, Dec 2011.

[48] E. A. Mistonova and O. Y. Andreev, "Calculation of the cross section of radiative double-electron capture by a bare nucleus with emission of one photon," *Phys. Rev. A*, vol. 87, p. 034702, Mar 2013.

[49] "NIST atomic spectra database ionization energies form." https://physics.nist.gov/PhysRefData/ASD/ionEnergy.html. Accessed: 2019-09-19.

[50] "Electron binding energies, in electron volts, for the elements in their natural forms.." http://xdb.lbl.gov/Section1/Table_1-1.pdf. Accessed: 2019-09-19.

[51] R. Middleton, "A survey of negative ions from a cesium sputter source," *Nuclear Instruments and Methods in Physics Research B*, vol. 144, no. 3, pp. 373–399, 1977.

[52] J. H. Billen and H. T. Richards, "SNICS: A source of negative ions by cesium sputtering," *SNEAP 78: Symposium of Northeastern Accelerator Personel*, vol. 10, no. 24, 1979.

[53] R. J. V. de Graaff, K. T. Compton, and L. C. V. Atta, "The electrostatic production of high voltage for nuclear investigations," *The Physical Review*, vol. 43, no. 3, pp. 149–157, 1933.

[54] F. T. Howard, *Tandem Accelerators-1973-74*. Oak Ridge National Laboratory, 1974.

[55] A. Kern. personal communication.

[56] J. A. Tanis, *Handbook for Highly Charged Ion Spectroscopic Research*. CRC Press, 1st ed., 2011.

[57] "NSCL data acquisition documentation." http://docs.nscl.msu.edu/daq/. Accessed: 2019-09-24.

[58] F. Hopkins, R. L. Kauffman, C. W. Woods, and P. Richard, "K x-ray transitions in one- and two-electron oxygen and fluorine projectiles produced in helium, neon, and argon targets," *Physical Review A*, vol. 9, no. 6, pp. 2413–2420, 1974.

[59] P. N. S. Kumara. Ph.D. Dissertation, Western Michigan University 2018.

[60] W. E. Meyerhof, R. Anholt, J. Eichler, H. Gould, C. Munger, J. Alonso, P. Thieberger, and H. E. Wegner, "Atomic collisions with relativistic heavy ions. III. electron capture," *Phys. Rev. A*, vol. 32, pp. 3291–3301, Dec 1985.

[61] R. Anholt *et al.*, "Observation of radiative capture in relativistic heavy-ion—atom collisions," *Phys. Rev. Lett.*, vol. 53, pp. 234–237, Jul 1984.

[62] S. Tashenov *et al.*, "First measurement of the linear polarization of radiative electron capture transitions," *Phys. Rev. Lett.*, vol. 97, p. 223202, Nov 2006.

[63] A. I. Mikhailov, I. A. Mikhailov, A. V. Nefiodov, G. Plunien, and G. Soff, "Correlated double-electron capture with emission of a single photon," *Physics Letters A*, vol. 328, pp. 350–356, 1995.